ORIGINAL PAPER

Temperature and pressure effects on the structural and vibrational properties of forsterite from density functional theory studies

Sha Chen[1,2] · Udo Becker[1]

Abstract

Due to experimental challenges and computational complexities, limited research has explored high-temperature and high-pressure conditions on mineral vibrations. This study employs the quasi-harmonic approximation (QHA) and density functional theory (DFT) to investigate the impact of temperature and pressure on the structural properties and infrared and Raman vibrational modes of forsterite. The computational process involves determining lattice parameters, optimizing the internal crystal structure, and calculating IR and Raman spectra at various temperature and pressure values, both separately and combined. Results highlight significant anisotropy in forsterite, with the b-axis being most sensitive to temperature and pressure, followed by the c-axis, while the a-axis exhibits greater stiffness. The positions of vibrational modes typically shift to higher frequencies with increasing pressure (average shift of 2.70 ± 1.30 cm^{-1}/GPa) or to lower frequencies with increasing temperature (average shift of -0.017 ± 0.018 cm^{-1}/K). Modes associated with SiO$_4$ stretching and bending are less affected by temperature or pressure than translational and rotational modes. A brief investigation into isotope and chemical substitution, as well as cation distribution, in the solid solution (Mg, Fe)$_2$SiO$_4$ reveals lower wavenumbers in fayalite modes compared to forsterite modes, attributed to the heavier Fe mass and larger cell parameters. This study establishes a methodology for computing vibrational frequencies under simultaneous temperature and pressure and emphasizes the significant impact of various factors on vibrational modes. Caution is advised when using vibrational modes for identifying compositions within solid solutions.

Introduction

Infrared (IR) and Raman spectroscopy rely on the interaction of nuclei with electromagnetic radiation (vibrations of atoms/bonds). IR spectroscopy entails the absorption of specific frequencies, whereas Raman spectroscopy involves inelastic scattering. The resulting infrared and Raman spectra capture lattice vibrations, reflecting the combined influence of chemical compositions and structures. These unique spectra facilitate the identification and characterization of materials, making them invaluable in Earth and planetary sciences. With advancing techniques, IR and Raman spectroscopy have not only contributed to the studies of earth and extraterrestrial samples but have also expanded their applications to remote planetary exploration (Karr 1975; Wang et al. 1995; Cooney et al. 1999; Ling et al. 2011; Kayama et al. 2018). Various space missions, such as the Mars 2020 Perseverance rover, ExoMars rover, and the Martian Moons eXploration mission, equip Raman spectrometers for mineral identification, composition analysis on planetary surfaces, and the search for evidence of life (Korablev et al. 2017; Rull et al. 2017; Cho et al. 2021; Lalla et al. 2022).

However, despite their versatile applications, several constraints limit the widespread use of infrared and Raman spectra. One notable limitation is the insufficient availability of databases for various minerals. Vibrational spectra are highly sensitive to even minor perturbations within

✉ Sha Chen
  chensha@epss.ucla.edu

1 Department of Earth and Environmental Sciences, University of Michigan, 1100 North University Avenue, Ann Arbor, MI 48109, USA

2 Department of Earth, Planetary, and Space Sciences, University of California, Los Angeles, 595 Charles E Young Dr E, Los Angeles, CA 90095, USA

chemical bonds, influenced by factors such as temperature, pressure, chemical composition, isotopic substitution, cation distribution, and spin states. To effectively utilize these spectra for mineral identification and differentiation, a thorough examination of the impact of each factor on vibrational modes is essential.

This study focuses on olivine, a common rock-forming mineral found in many planetary bodies (Earth, Moon, Mars, Mercury, etc.). The structural and vibrational properties of olivine have been extensively studied through both experimental and physical–mechanical computations (Iishi 1978; Akaogi et al. 1984; Hofmeister 1987; Rao et al. 1988; Chopelas 1990, 1991; Gillet et al. 1991; Ghose et al. 1992; Wang et al. 1993; Gillet 1996; Noel et al. 2006; Li et al. 2007; McKeown et al. 2010; Stangarone et al. 2017). However, most studies of infrared absorption and Raman spectroscopy for olivine have been conducted either under ambient conditions (Paques-Ledent and Tarte 1973; Iishi 1978; Hofmeister 1987, 1997; Kuebler et al. 2006; Dyar et al. 2009), high pressure at room temperature using diamond-anvil cells (Besson et al. 1982; Chopelas 1990; Durben et al. 1993), or high temperature using a heating stage at ambient pressure (Kolesov and Geiger 2004). To our knowledge, there are no published studies on simultaneous changes in temperature and pressure for olivine due to difficulties in experimental setup and computational modeling.

The experimental setup for simultaneous changes in temperature and pressure poses significant challenges. Computational methods provide a complementary approach for studying high-temperature and high-pressure mineral properties, allowing a deeper understanding of macro-properties at the atomic level and visualization of each normal mode. While simulating high pressures is relatively straightforward, simulating high temperatures requires careful consideration of anharmonicity. Before the temperature reaches levels where anharmonicity becomes significant, the QHA is accurate enough to model the temperature effect. Additionally, changes in temperature and pressure mainly affect the vibrational frequencies of a crystal by altering cell parameters and internal coordinates when anharmonicity is insignificant. Therefore, three steps are taken to compute the vibrational modes: using QHA to obtain cell parameters under temperature and pressure, performing geometry optimizations under fixed cell parameters to optimize the internal coordinates of atoms, and lastly, computing the vibrational frequencies of infrared and Raman. Additionally, we briefly examine the isotope and chemical compositional effect and cation ordering on the vibrational frequencies.

This study is based on Chapter 3 of S.C.'s thesis (Chen 2022).

Vibrational modes and crystal symmetry

Olivine belongs to the orthorhombic crystal system with the point group mmm in Hermann-Mauguin notation or D2h in the Schönflies notation. The space group is Pbnm, a non-conventional setting of Pnma with space group number 62. The chemical formula for olivine can be expressed as $M1M2SiO_4$, featuring two non-equivalent types of octahedral sites, $M1O_6$ and $M2O_6$. There are four formula units in the unit cell, resulting in multiplicities of 4 for both octahedral sites. The M1 octahedron is distorted and smaller than M2. The most common metal cations occupying the octahedral sites are Fe and Mg. Due to the similar ionic radii of Fe and Mg, they form a complete solid solution, with the two end members being forsterite Mg_2SiO_4 and fayalite Fe_2SiO_4. A unit cell comprises 28 atoms, leading to 84 vibrational modes corresponding to the total degree of freedom. The symmetry decomposition of the 84 normal modes at the center of the Brillouin zone Γ, derived theoretically, is

$$\begin{aligned}\Gamma_{\text{total}} =\ &11A_g + 11B_{1g} + 7B_{2g} + 7B_{3g} \\ &+ 10A_u + 10B_{1u} + 14B_{2u} + 14B_{3u}\end{aligned} \tag{1}$$

A Brillouin zone represents the primitive cell of a crystal in its reciprocal space. Mulliken symbols, such as A_g, B_{1g}, etc., denote different symmetry types or irreducible representations. The character table of a point group provides information on which irreducible representations are infrared-active or Raman-active. Irreducible representations corresponding to linear functions, namely B_{1u}, B_{2u}, and B_{3u}, are infrared active, while those corresponding to quadratic functions, A_g, B_{1g}, B_{2g}, and B_{3g}, are Raman active. Symmetry A_u modes remain silent. In total, there are 35 IR-active and 36 Raman-active vibrational modes. Three of these (acoustic) modes involve translations of the entire system ($B_{1u} + B_{2u} + B_{3u}$).

$$\Gamma_{\text{infrared}} = 9B_{1u} + 13B_{2u} + 13B_{3u} \tag{2}$$

$$\Gamma_{\text{Raman}} = 11A_g + 11B_{1g} + 7B_{2g} + 7B_{3g} \tag{3}$$

The olivine structure consists of isolated SiO_4 tetrahedra and two different MgO_6 octahedra. The tetrahedra exhibit three different Si–O distances, and their skewing is induced by the Coulomb force exerted by Mg on Si and O atoms (Lam et al. 1990). Each of the two Mg-octahedra has three distinct Mg1–O distances and four distinct Mg2–O distances.

Aside from the three acoustic modes, the remaining vibrational modes can be attributed to the translations of M1, M2, and SiO_4, as well as the rotation and internal movement of SiO_4. The internal movements of SiO_4,

involving bending and stretching, can be categorized into four types based on their symmetries: ν_1, ν_2, ν_3, and ν_4 (Lam et al. 1990). The ν_1 and ν_2 modes represent symmetric stretching and bending of the Si–O bond, respectively, with the Si atom remaining stationary. The ν_3 and ν_4 modes are antisymmetric stretching and bending modes, respectively, with the Si atom not stationary. The type of vibration is correlated with the symmetry derived from the correlation method and is summarized in Table 1 (Paques-Ledent and Tarte 1973; Hofmeister 1987).

Methods

Temperature and pressure effects on vibrational frequencies and QHA

The dependence of a given frequency on temperature and pressure can be caused by two aspects: (1) volume change due to compressibility (P) and thermal expansion (T); (2) a volume-independent contribution from lattice anharmonicity (T) (Gillet et al. 1989; Dai et al. 2013; Deshpande et al. 2014). At lower temperatures when anharmonicity is negligible, vibrational frequencies, with fixed composition, are a function of volume (Liu 1993; Gillet 1996). However, at very high temperatures, the interaction between phonons becomes significant, necessitating non-static methods, such as molecular dynamics and Monte Carlo. While these methods can be useful, they are strictly only valid for solids at elevated temperatures as they neglect the effect of vibrational quantum effects such as the zero-point energy. Therefore, anharmonicity must be checked in order to determine if QHA is a valid approximation. Gillet et al. (1989) stated

that the anharmonic effect for mantle minerals becomes noticeable above 1000 K, leading to a 2% difference in heat capacity, C_v, at 1000 K and a 7% difference at 2000 K. Their experiments were conducted at room pressure. The valid domain of QHA in temperature increases with higher pressure (Carrier et al. 2007). Several studies (Baroni et al. 2010; Dovesi et al. 2018; Allen 2020) show that simulation with QHA is remarkably accurate in a wide temperature range up to close to the melting line. The temperature and pressure range of olivine in the upper mantle is approximately 1800 °C and 14 GPa. Since our simulations never exceed this range, the temperature and pressure conditions simulated in this study should be accurate enough using QHA. Erba et al. (2015a) also concluded that the QHA is reliably accurate in describing the thermodynamic properties of forsterite within its entire stability domain, as evidenced by comparing their computational results with experimental data from the literature.

Another approach to evaluate anharmonicity is by using the parameter mode anharmonicity, a_i, defined as $a_i = \left(\frac{\partial ln(\nu_i)}{\partial T} \right)_V$ (Gillet et al. 1989). If a_i is not equal to 0, it indicates anharmonicity. Gillet (1996) concluded that the parameter a_i typically ranges from $-1 \cdot 10^{-5}$ to $-1 \cdot 10^{-4}$ K^{-1} in various silicates and under different high-temperature and high-pressure conditions. The absolute value tends to be larger for low wavenumber modes, typically lattice modes. To estimate the effect of anharmonicity on vibrational frequencies, consider the following calculation. Suppose a_i is near the maximum of measured experimental data, i.e., -10^{-4} K^{-1}. When the volume is constant (i.e., the pressure and temperature effect cancel each other out, keeping the volume unchanged), the frequency change increases with

Table 1 Classification of normal modes (81) of olivine for Pbnm, excluding the three acoustic modes

	Raman				Infrared			Silent
	A_g	B_{1g}	B_{2g}	B_{3g}	B_{1u}	B_{2u}	B_{3u}	A_u
SiO$_4$ internal (N = 36)								
$\nu1$	1	1	0	0	0	1	1	0
$\nu2$	1	1	1	1	1	1	1	1
$\nu3$	2	2	1	1	1	2	2	1
$\nu4$	2	2	1	1	1	2	2	1
Total	6	6	3	3	3	6	6	3
Rotation (N = 12)								
SiO$_4$ rotation	1	1	2	2	2	1	1	2
Translation (N = 33)								
SiO$_4$ translation	2	2	1	1	0	1	1	1
M1 translations	0	0	0	0	3	3	3	3
M2 translations	2	2	1	1	1	2	2	1
Total	4	2	4	2	4	6	6	5

temperature change. For instance, if the temperature change is 1000 K, the relative change of v_i would be approximately 10%. This offset caused by anharmonicity is acceptable when the temperature is below 1000 K, as it may be smaller than the computational error.

The QHA serves as a reliable approximation at low temperatures, before temperatures become high enough to exhibit anharmonic behavior. QHA finds widespread use in studying thermal properties and the temperature effects on vibrational frequencies (Reynard et al. 1992; Li et al. 2007; Wu and Wentzcovitch 2007; Deringer et al. 2014; Wen et al. 2017). QHA is expected to be a valid approximation for most of the mantle and only becomes problematic near the core-mantle boundary based on the measured melting temperature and expected mantle temperature (Wentzcovitch et al. 2010). QHA assumes that all bonds within a given crystal volume behave harmonically, with the equilibrium length capable of changing. Additionally, it posits that temperature and pressure impact vibrational frequencies solely through volume changes. However, it's crucial to note that this assumption is only strictly accurate for cubic structures. Anisotropy in compressibility and thermal expansion has been reported for olivine in the literature (Andrault et al. 1995; Trots et al. 2012). Beyond cell parameters, accurate fractional coordinates of atoms in the unit cell are equally crucial. Maintaining static fractional coordinates while adjusting cell parameters leads to incorrect proportional changes in all bond lengths, as observed in experimental data. SiO_4 tetrahedra exhibit more rigidity than MgO_6 octahedra. Hazen (1976) concluded that the thermal expansion and compressibility of Mg octahedra are comparable to those of bulk forsterite, while the stronger Si–O bonds undergo minimal expansion or compression. Therefore, this study considers the optimization of both cell parameters and fractional coordinates at the equilibrium cell volume.

Calculation of vibrational frequencies under changing *T* and *P* conditions

In this study, we conducted three series of calculations to examine the temperature and pressure effect: (1) pressure up to 15 GPa at static temperature (0 K); (2) temperature up to 900 K at static pressure (no hydrostatic pressure) to avoid anharmonicity; (3) simultaneous temperature and pressure. The computation is relatively straightforward for the sole pressure effect at 0 K. The optimized structure under external hydrostatic pressure can be easily obtained, and then the vibrational frequencies can be computed. When the temperature changes, the QHA must be used to obtain the volume (only cell parameters *a*, *b*, and *c*, no internal coordinates) under *T* and *P* first. This is followed by geometry optimization of the internal atomic positions while fixing the cell parameters, and finally, infrared and Raman

frequencies are computed for the optimized structure. The pressure at a given volume *V* and temperature *T* has two parts: $P(V, T) = P(V_0 \rightarrow V)_{T=T_0} + P_{th}(T_0 \rightarrow T)_V$. The first term is the pressure needed to change the volume at a reference temperature, and the second term is thermal pressure, defined as the pressure change at constant volume V due to the temperature change.

Our ultimate goal is to compute infrared and Raman spectra under simultaneous *T* and *P* changes, where relevant data from both experiments and computations is lacking. Olivine, a dominant mineral phase in Earth's upper mantle down to the 410-km seismic discontinuity, undergoes a phase transition at this depth from α-$(Mg, Fe)_2SiO_4$ (olivine) to β-$(Mg, Fe)_2SiO_4$ (wadsleyite). The pressure at 410 km is approximately 14 GPa, while determining the temperature is more challenging. Various methods provide different temperature estimates, but it is approximately 1800 K (Akimoto et al. 1976; Ito and Katsura 1989; Trubitsyn and Trubitsyn 2020). For forsterite, the phase transition occurs at 1600 °C (1873 K) at 15 GPa and at 1200 °C (1473 K) at 14 GPa (Katsura and Ito 1989). Considering the stability range of forsterite, we selected the following temperature/pressure pairs: (1000 K, 5 GPa), (1500 K, 5 GPa), (1500 K, 10 GPa), and (2000 K, 10 GPa).

The Crystal17 program is employed for the DFT + QHA computations (Erba 2014; Erba et al. 2015a, b, c). As discussed earlier, vibrational frequencies under changing temperature and pressure are essentially a function of equilibrium geometry, under the temperature and pressure ranges we consider. Therefore, geometry optimizations under specific pressures or temperatures precede respective frequency computations. The initial forsterite structure is obtained from Bostroem (1987) with cell parameters of 4.749 Å, 10.1985 Å, and 5.9792 Å. The functional B3LYP is employed, which is a hybrid between a Hartree–Fock approach for the exchange term, and a BLYP functional for correlation. The basis sets used are 8-511d1G_valenzano_2006 for Mg (Valenzano et al. 2007), 86-311G for Si (Pascale et al. 2005; Noel et al. 2006), and 8-411d11G for O (Valenzano et al. 2006). The default isotopes used in the frequency calculations are 23.9850 for Mg, 27.9769 for Si, and 15.9949 for O.

Vibrational frequencies are computed at the Γ point of the reciprocal unit cell within the harmonic approximation at static temperature and pressure. The Hessian matrix, H_{ij}, represents the second derivative matrix of energy due to the displacement of any atom from its equilibrium position. The mass-weighted Hessian matrix is calculated from the dynamic matrix divided by the square root of the mass of any given atom pair. The eigenvalues of the mass-weighted dynamic matrix are the frequencies, and the eigenvectors are the normal modes. Transverse optical (TO) modes are computed by default, and both infrared and Raman frequencies

and intensities are calculated. Harmonic vibrational frequencies are computed and fitted for different volumes, with four volumes used by default. Once the equations of frequencies with volume are determined, all other thermodynamic properties can be analytically derived by minimizing the free energy. For example, the Helmholtz free energy F of the system in QHA can be expressed as a function of crystal structure X and temperature T:

$$F(X,T) = U(X) + \sum_i \frac{1}{2} h\nu_i(X) + k_B T \sum_i ln\left(1 - e^{-\frac{h\nu_i(X)}{k_B T}}\right) \quad (4)$$

where the three terms are the internal energy of the system ($U(X)$), the zero-point vibrational energy $\left(\sum_i \frac{1}{2} h\nu_i(X)\right)$, and the temperature effect of the vibration part $\left(k_B T \sum_i ln\left(1 - e^{-\frac{h\nu_i(X)}{k_B T}}\right)\right)$.

Results

Crystal structure changes with temperature and pressure

The crystal structure of forsterite was examined under changing temperature and pressure to explore its thermal expansion and compressibility, respectively. Table 2 presents the computed cell parameters and volume data for various temperature and pressure combinations. Cell parameters and volume with a single parameter change (either pressure or temperature) are plotted and compared to the literature data

in Fig. 1. To emphasize unit cell changes resulting from variations in pressure and temperature conditions only, we have normalized the data by plotting the ratios of the cell parameters at a given temperature and pressure divided by those under ambient conditions (300 K, 0 GPa). This normalization eliminates subtle differences in initial cell parameters due to the computational parameters chosen, focusing on the impact of changes in pressure and temperature. Our calculated data demonstrate good agreement with the literature data.

To assess changes in volume and cell parameters in response to temperature and pressure, two crucial parameters come into play: bulk modulus and thermal expansion coefficient. Bulk modulus serves as a metric for gauging the volume change resistance to pressure, reflecting the material's compressibility. The thermal expansion coefficient delineates the volume variation induced by temperature fluctuations. Specifically, the isothermal bulk modulus, denoted as K_T, is defined as

$$K_T = -V\left(\frac{\partial P}{\partial V}\right)_T = -\left(\frac{\partial P}{\partial lnV}\right)_T \quad (5)$$

The adiabatic bulk modulus, K_S, is defined analogously but under adiabatic conditions, signifying a process without heat exchange. Compressibility is the reciprocal of bulk modulus. The bulk thermal expansivity, denoted as α, is defined as

$$\alpha = \frac{1}{V}\left(\frac{\partial V}{\partial T}\right)_P = \left(\frac{\partial lnV}{\partial T}\right)_P \quad (6)$$

and the linear thermal expansivity α_i is defined as

$$\alpha_i = \frac{1}{x_i}\left(\frac{\partial x_i}{\partial T}\right)_P = \left(\frac{\partial lnx_i}{\partial T}\right)_P \quad (7)$$

where x_i is the cell parameter.

The logarithm of volume exhibits a correlation with cell parameters, prompting the utilization of logarithmic fitting for the data presented in this study, as illustrated in Fig. 1. To capture the intricate relationship, a second-order polynomial is employed instead of a linear function for the expansion range of pressure and temperature. Notably, the considerably smaller coefficients in the T^2 and P^2 terms, two to four orders of magnitude lower than the linear terms, allow for a meaningful comparison of compressibility and linear thermal expansivity along different axes of olivine.

Compression and thermal expansion exert opposing influences on cell parameters; an increase in pressure diminishes cell volume, while elevated temperature produces the opposite effect. The rates of change with respect to pressure (dln/dP) for the a, b, and c axes are -0.0018, -0.0034, and -0.0026 GPa^{-1} at 0 GPa, respectively. This indicates that compressibility is highest along the b-axis, followed by c

Table 2 Unit-cell parameters of forsterite calculated under varying temperature (in K) and pressure (in GPa)

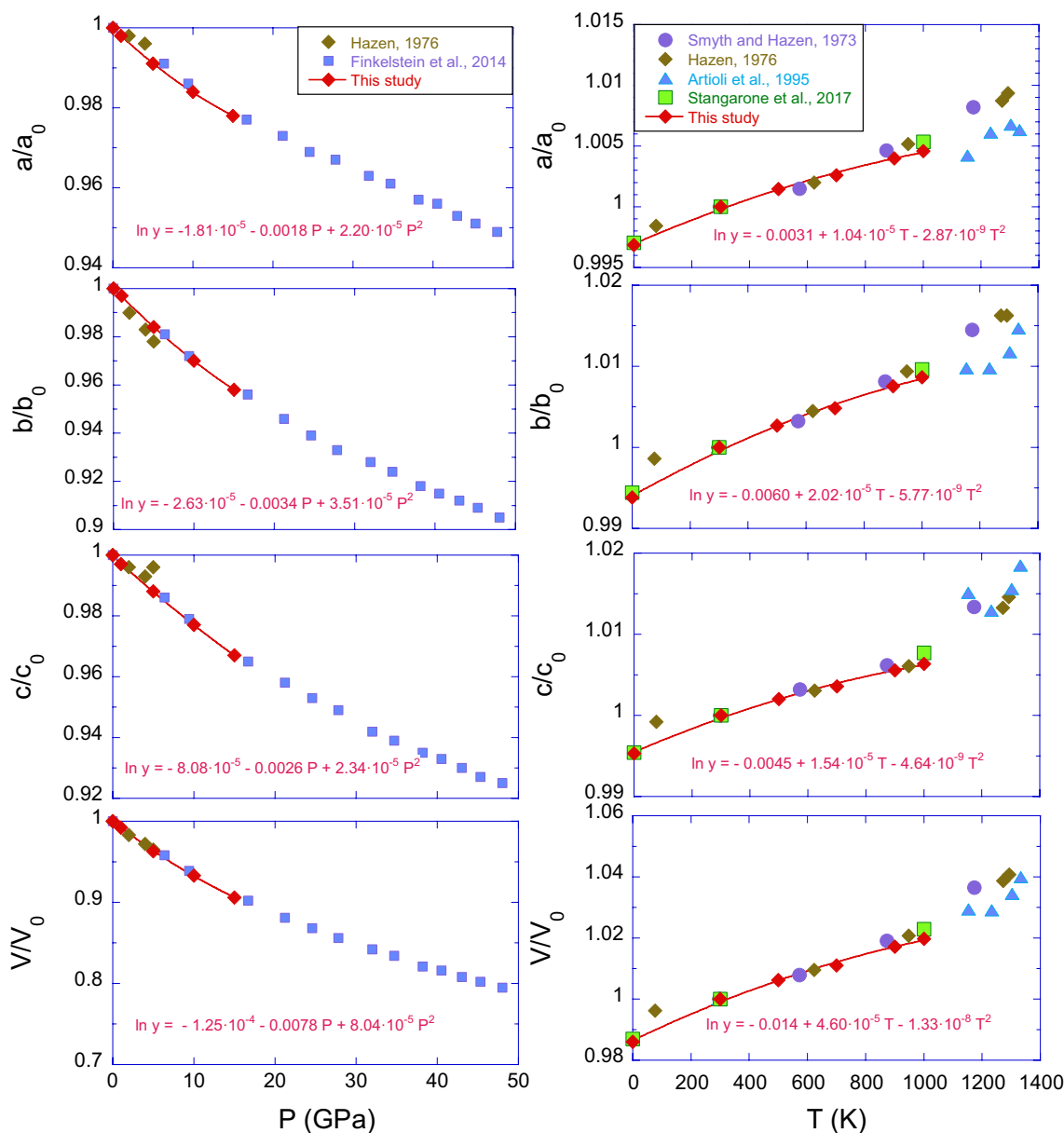| Temperature (K)	Pressure (GPa)	Cell parameters			Volume (Å^3)
		a (Å)	b (Å)	c (Å)	
0	0	4.791	10.295	6.016	296.7
0	1	4.782	10.259	6.000	294.4
0	5	4.750	10.129	5.942	285.9
0	10	4.715	9.984	5.877	276.7
0	15	4.685	9.858	5.818	268.7
300	0	4.806	10.359	6.045	300.9
500	0	4.813	10.386	6.057	302.8
700	0	4.818	10.409	6.066	304.2
900	0	4.825	10.437	6.078	306.1
1000	0	4.828	10.448	6.083	306.8
1000	5	4.791	10.297	6.018	296.9
1500	10	4.772	10.219	5.984	291.8
1500	5	4.809	10.369	6.050	301.6
2000	10	4.789	10.288	6.014	296.3
2000	20	4.726	10.024	5.894	279.2

Fig. 1 Lattice parameter changes with pressure (left panel) and temperature (right) in this study are compared with the literature. Cell parameters (a, b, c) and volume (V) are normalized by dividing them by their respective values at ambient conditions (a_0, b_0, c_0, V_0) to eliminiate subtle differences in initial cell parameters. A second-order polynomial equation is used to fit the logarithm of cell parameters or volume with pressure or temperature. Only data from this study is used for the fitting

and a, aligning with findings in the literature (Andrault et al. 1995; Finkelstein et al. 2014). Similarly, the rates of change with respect to temperature ($d\ln/dT$) for the a, b, and c axes are 1.04×10^{-5}, 2.02×10^{-5}, 1.54×10^{-5} K^{-1} at 0 K, representing linear thermal expansion at 0 K. Axis b is the most temperature sensitive, followed by c and a, mirroring the order of compressibility (Erba et al. 2015a).

The system's two bulk moduli, K_S and K_T, are computed in this study at various pressures and temperatures by minimizing the second derivative of energy with respect to volume.

The results are presented in Table 3 and Fig. 2. Notably, the values of K_S and K_T coincide only at zero temperature, with K_S consistently exceeding K_T at any finite temperature. The bulk modulus and its derivative to pressure, computed by fitting the third-order Birch-Murnaghan equation at 0 K and 0 GPa are 123.5 GPa and 4.35, respectively, demonstrating close agreement with literature values (Table 3). The bulk modulus at 0 K is reported at different pressures, and a linear fit reveals the relationship $K = 123.3 + 4.30P$ (in GPa). This value falls within the reported range of literature values,

Table 3 Comparison of bulk modulus calculated in this study with literature data

References	Compo	$K_{T=298K}$	K_S	$K_{T=298K}'$	$K_{T=0\,K}$	$K_{T=0\,K}'$	Methods
This study	Fo	115.7		4.35	123.5	4.35	DFT + QHA simulation
Nestola et al. (2011)	Fo−Fa	124.7 ± 0.9		5.3 ± 0.3			Single-crystal XRD
Poe et al. (2010)	Fo	124.4		4.9			Single-crystal XRD
Couvy et al. (2010)	Fo	129.6 ± 3.2					Macro-powder XRD
Couvy et al. (2010)	Fo	123.3 ± 3.4					Nanocrystalline XRD
Abramson et al. (1997)	Fo$_{90}$	126.3	129.4	4.28			Sound velocity
Zha et al. (1996)	Fo	128.8		4.2			Sound velocity
Downs et al. (1996)	Fo	125		4			Single-crystal XRD
Andrault et al. (1995)	Fo− Fa	131		4			Single-crystal XRD measurements
Kudoh and Takéuchi (1985)	Fo	123		4.3			Single-crystal XRD
Suzuki et al. (1983)	Fo	127.6	128.9				Rectangular parallelepiped resonance
Hazen (1977)	Fo	113		4			Single-crystal XRD
Hazen (1976)	Fo	132		4			Single-crystal XRD

Fo = Mg$_2$SiO$_4$. Fa = Fe$_2$SiO$_4$. Compo. denotes composition

Fig. 2 **a** Bulk modulus at various pressures at 0 K with displayed linear fitting equation. **b** Isothermal and adiabatic bulk modulus at different temperatures with shown second-order polynomial equation
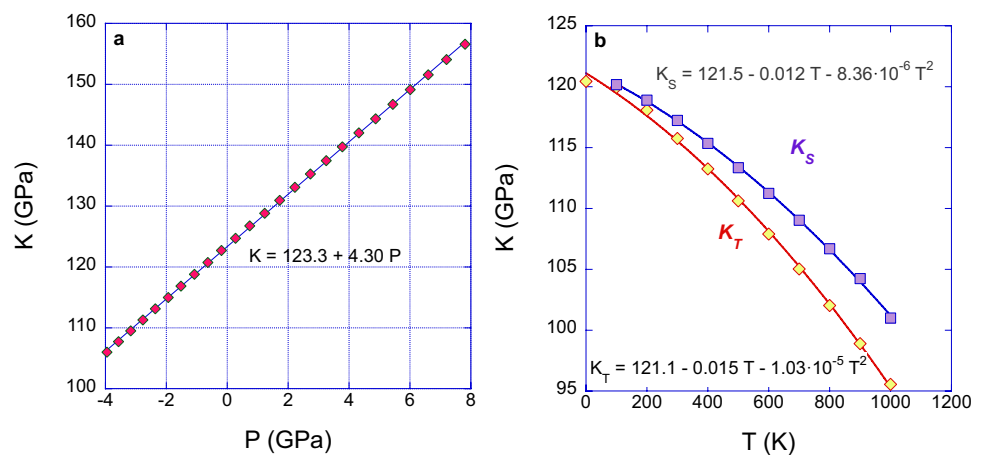
which exhibits significant variability. The K_T and K_S data at different temperatures are also provided. To characterize the bulk modulus as a function of temperature, a second-order polynomial is employed to fit K_S and K_T with T, resulting in Eqs. 8 and 9:

$$K_T = 121.1 - 0.015\,T - 1.03 \times 10^{-5}\,T^2 \tag{8}$$

$$K_S = 121.5 - 0.012\,T - 8.36 \times 10^{-6}\,T^2 \tag{9}$$

In this study, both volumetric and linear thermal expansion coefficients are computed up to 1000 K. The thermal expansivity increases with temperature while the rate of change $\frac{\partial \alpha}{\partial T}$ decreases with temperature, as illustrated in Fig. 3. Forsterite exhibits pronounced anisotropy, with $\alpha_b > \alpha_c > \alpha_a$, indicating that axis a is the most rigid among the three axes. Several equations describing the thermal expansion

coefficient with temperature have been proposed. Our data is fitted using the equation $\alpha = a_0 + a_1 \times T + a_2/T^2$, and the results are compared with literature values (Table 4).

The bond lengths in the crystal structures for various temperature and pressure conditions are plotted in Fig. 4. The ratio is used in reference to the 0 K or 0 GPa conditions. Generally, Mg2–O bonds exhibit higher sensitivity to changes in pressure and temperature than Mg1–O bonds, while Si–O bonds display the smallest sensitivity.

For thermal expansion, different Mg–O expansions with temperature vary from $(1.7 \pm 0.2) \times 10^{-5}$ to $(5.1 \pm 0.5) \times 10^{-5}$ Å/K with the average of 2.9×10^{-5} Å/K, which agrees well with the value range of 2–5×10^{-5} Å/K in Hazen (1976). The temperature effect on Si–O, however, is less pronounced. The Si–O bond lengths initially increase with temperature up to 700 K, followed by a decrease at a temperature of 900 K, though the variations are modest. Linear fitting yields the expansion rate of Si–O
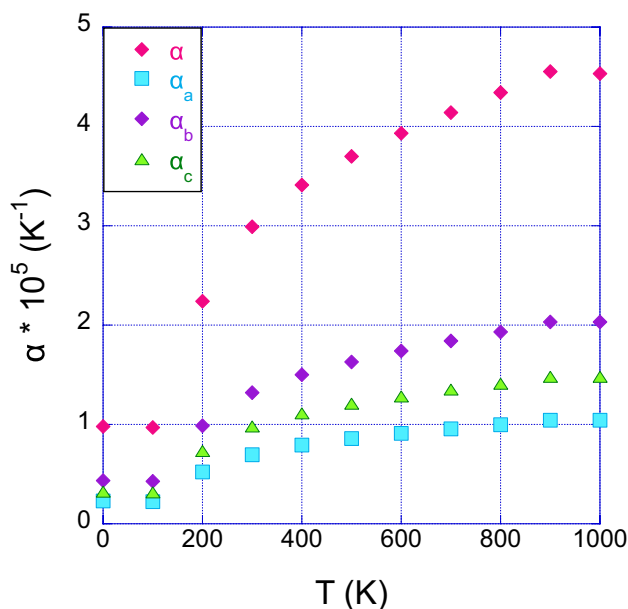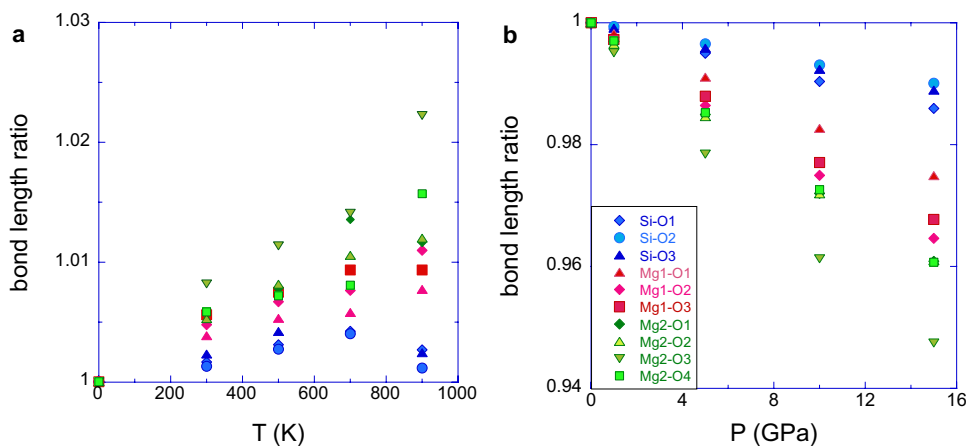
Fig. 3 Thermal expansion (α) and linear thermal expansion coefficients (α_a, α_b, and α_c). The connection between the bulk and linear thermal expansion coefficients is $\alpha_V = \alpha_a + \alpha_b + \alpha_c$

Table 4 Comparison of thermal expansion coefficient equations from this study and literature

	T (K)	$10^5 a_0$	$10^8 a_1$	a_2
This study (with $1/T^2$ term)	0–1000	1.96	2.28	1.81
Kumazawa and Anderson (1969)		2.47	4.7	
Hazen (1976)	298–1293	2.56		
Suzuki et al. (1983)	298–1213	2.48		
Gillet et al. (1991)	300–2000	2.77	0.97	–0.32
Bouhifd et al. (1996)	300–2150	2.832	0.758	
Trots et al. (2012)	297–1313	3.23	0.63	

The coefficients α_0, α_1, and α_2 correspond to the equation $\alpha = a_0 + a_1 \times T + a_2/T^2$

from $(2.3 \pm 4.8) \times 10^{-6}$ to $(6.1 \pm 2.5) \times 10^{-6}$ Å/K, with an average of 4.1×10^{-6} Å/K. The expansion of Mg–O is approximately seven times higher than that of Si–O. Hazen (1976) concludes that Si–O neither expands nor compresses significantly with temperature, while the change in Mg–O is comparable to the volume change. The limited change observed in Si–O bonds with temperature is attributed to the presence of isolated tetrahedra in olivine. In silicates, the bond lengths and volumes for tetrahedra with four bridging O atoms seem to increase with temperature more rapidly than those with four non-bridging O atoms.

The Mg–O compression with pressure varies from $(-7.7 \pm 0.4) \times 10^{-3}$ to $(-3.5 \pm 0.06) \times 10^{-3}$ Å/GPa with an average of -5.4×10^{-3} Å/GPa. In comparison, the compression rate for Si–O varies from $(-1.5 \pm 0.02) \times 10^{-3}$ to $(-1.0 \pm 0.02) \times 10^{-3}$ Å/GPa with an average of -1.29×10^{-3} Å/GPa. On average, the compression of Mg–O is approximately four times higher than Si–O.

Under conditions resembling the Earth's interior, compression due to pressure has a more pronounced effect on olivine cell parameters and bond lengths than thermal expansion. Taking the pressure at the 410 km discontinuity to be 14 GPa and the temperature around 1800 K, the average Mg–O bond changes by -0.0756 Å due to pressure and lower bond change due to temperature (0.0522 Å). The same is true for Si–O bonds and volume, resulting in generally smaller volumes and bond lengths at greater depths.

Considering the change in bond length relative to volume, from 0 to 900 K, the volume change is 3.2%. Si–O experiences a 0.21% change, while Mg1–O and Mg2–O change by 0.9% and 1.54%, respectively. With pressure ranging from 0 to 15 GPa, the volume change is -9.4%. Si–O exhibits a -1.2% change, while Mg1–O and Mg2–O bonds change by -3.1% and -4.2%, respectively.

Fig. 4 **a** Bond lengths ratios (bond length at a given T/ bond length at 0 K) change with temperature for calculated structures in this study for forsterite; **b** bond lengths ratios (bond length at given P/bond length at 0 GPa) with pressure. Blue, green, and red symbols represent Si–O, Mg2–O, and Mg1–O, respectively

Comparison of vibrational spectra with the literature and mode assignments

Infrared and Raman spectra have been intensely investigated by FTIR and Raman spectroscopy, along with computational methods. However, most studies have focused on ambient temperature and pressure conditions through experimental measurements and static calculations (0 K, 0 GPa). This study compares infrared and Raman frequencies calculated at 300 K and 0 GPa with experimental data from various sources. Frequencies calculated at static conditions are compared with computational data found in the literature (Tables 5 and 6). The IR and Raman spectra are consistent with the literature in general. However, even the

Table 5 Comparison of infrared vibrational frequencies with literature and mode assignments

	This study			Noel (2006)		Hofmeister (1987)			Iishi (1978)		
	TO	TO	Mode	TO	LO	TO	LO	Mode	TO	LO	Mode
	0 K	300 K									
B1u											
1	210	205	T(Mg1)	207	207	276	276	T(M2)	201		T(M1)
2	279	268	T(Mg1, Mg2)	278	279	293	299	T(M1)	224		T(M1)
3	293	276	T(Mg1, Mg2)	290	313	309	313	T(M1)	274	278	T(M1, M2)
4	310	291	R(SiO$_4$), T(Mg)	313	320	365	371	T(M1)	296	318	T(M1)
5	416	395	R(SiO$_4$)	420	426	412	450	R?	365	371	R(SiO$_4$)
6	424	409	R(SiO$_4$), T(Mg1)	428	461	463	482	R	423	459	R(SiO4)
7	489	476	ν2	490	499	502	538	ν2	483	489	ν2
8	512	502	ν4	514	592	543	573	ν4	502	585	ν4
9	886	867	ν3	874	1005	865	957	ν3	885	994	ν3
B2u											
1	206	192	T(Mg, SiO$_4$)	143	144	142	144	T(SiO$_4$)	144		T(M1, SiO$_4$)
2	271	265	T(Mg)	277	277	268	276	T(M2)	224		T(M2)
3	296	281	T(Mg2)	292	312	290	298	T(M1)	280	283	T(M1)
4	322	317	T(Mg, SiO$_4$)	350	387	300	308	T(M1)	294	313	T(M1, M2)
5	388	367	T(Mg), R(SiO$_4$)	403	417	345	375	T(M2)	352	376	T(M2)
6	410	398	T(Mg), R(SiO$_4$)	432	453	398	408	T(M1)	400	412	T(M1)
7	476	460	T(Mg), R(SiO$_4$)	465	495	418	438	R	421	446	R(SiO$_4$)
8	509	496	T(Mg), ν2	517	520	452	488	ν2	465	493	ν2
9	539	527	T(Mg), ν4	535	588	504	511	ν4	510	516	ν4
10	615	605	ν4	638	638	520	572	ν4	537	597	ν4
11	850	829	ν1	835	843	828	844	ν1	838	843	ν1
12	966	950	ν3	870	966	865	961	ν3	882	979	ν3
13	988	973	ν3	989	999	984	996	ν3	987	993	ν3
B3u											
1	141	135	T(Mg, SiO$_4$)	206	207	201	201	T(SiO$_4$)	201		T(M1, SiO$_4$)
2	279	265	T(Mg2)	275	276	275	276	T(M2)	224		T(M2)
3	294	278	T(Mg1)	294	300	294	298	T(M1)	274	276	T(M1, M2)
4	349	333	T(Mg2)	322	323	309	313	T(M1)	293	298	T(M1)
5	403	392	T(Mg1)	388	398	319	321	T(M2)	320	323	T(M1)
6	428	414	T(Mg1)	412	473	377	388	R?	378	386	T(M1)
7	464	448	T(Mg1), R(SiO$_4$)	476	482	405	430	T(M1)	403	469	R(SiO$_4$)
8	515	501	T(Mg), ν2	513	539	434	463	ν2	498	544	ν2
9	534	523	ν4	540	563	505	511	ν4	562	566	ν4
10	639	626	ν4	614	660	601	644	ν4	601	645	ν4
11	849	828	ν1	838	838	841	842	ν1	838	845	ν1
12	889	865	ν3	962	971	950	961	ν3	957	963	ν3
13	991	972	ν3	982	1086	988	991	ν3	980	1086	ν3

Noel2006: Noel et al. (2006); Hofmeister 1987: Hofmeister (1987); Iishi1978: Iishi (1978)

Table 6 Comparison of Raman vibrational frequencies with literature and mode assignments

	This study, calc			Iishi (1978)		Chopelas (1991)		Noel	McKeown	S2017
	0 K	300 K	Mode	Exp.	Mode	Exp.	Mode	Calc.	Exp.	Calc.
Ag										
1	66	109	T(Mg2, SiO$_4$)	183	T(M2, SiO$_4$)	183	T(SiO$_4$)	188	183	191
2	211	259	T(Mg2, SiO$_4$)	227	T(M2, SiO$_4$)	226	T(SiO$_4$)	234	227	234
3	306	296	T(Mg2, SiO$_4$)	305	T(M2, SiO$_4$)	304	T(M2)	307	305	315
4	327	314	T(Mg2)	329	T(M2)	329	R(SiO$_4$)	329	329	335
5	345	333	R(SiO$_4$)	340	R(SiO$_4$)	339	R(M2)	345	340	351
6	440	411	ν2	424	ν2	422	ν2	425	423	432
7	567	510	ν4	546	ν4	545	ν4	560	546	556
8	606	611	ν4	609	ν4	608	ν4	618	609	616
9	838	812	ν1	826	ν1	824	ν1 + ν3	819	826	819
10	856	858	ν3	856	ν3	856	ν1 + ν3	856	856	857
11	969	948	ν3	966	ν3	965	ν3	967	966	974
B1g										
1	222	216	T(Mg2, SiO$_4$)	192	T(M2, SiO$_4$)	220	T(SiO$_4$)	225	227	228
2	259	249	T(Mg2, SiO$_4$)	224	T(M2, SiO$_4$)	274	T(SiO$_4$)	260	275	263
3	313	301	T(Mg2, SiO$_4$)	260	T(M2, SiO$_4$)	318	R(SiO$_4$)	317	318	323
4	361	347	T(Mg2)	318	T(M2)	351	T(M2)	367	374	372
5	390	383	R(SiO$_4$)	418	R(SiO$_4$)	383	T(M2)	391	384	393
6	440	426	ν2	434	ν2	434	ν2	442	434	447
7	608	584	ν4	583	ν4	582	ν4	596	583	593
8	641	629	ν4	632	ν4	632	ν4	645	632	644
9	854	830	ν1	839	ν1	838	ν1 (+ν3)	835	839	834
10	874	857	ν3	866	ν3	866	ν3(+ν1)	866	866	867
11	981	963	ν3	976	ν3	975	ν3	979	976	985
B2g										
1	188	171	M2, R(SiO$_4$)	142	T(Mg2)	175	T(SiO$_4$)	183	175	195
2	298	288	R(SiO$_4$), M2	244	T(SiO$_4$)	242	R(SiO$_4$)	253	244	304
3	323	310	T(SiO$_4$), M2	324	R(SiO$_4$)	323	T(M2)	324	324	327
4	377	364	R(SiO$_4$)	368	R(SiO$_4$)	365	R(SiO$_4$)	373	368	388
5	419	406	ν2	441	ν2	439	ν2	451	441	424
6	615	596	ν4	588	ν4	586	ν4	608	588	605
7	940	920	ν4	884	ν3	881	ν3	883	882	929
B3g										
1	183	177	M2, R(SiO$_4$)	226	T(SiO$_4$)	286	T(SiO$_4$)	190	203	183
2	250	232	M2, R(SiO$_4$)	272	T(M2)	315	R(SiO$_4$)	303	272	257

Table 6 (continued)

	This study, calc			Iishi (1978)		Chopelas (1991)		Noel	McKeown	S2017
	0 K	300 K	Mode	Exp.	Mode	Exp.	Mode	Calc.	Exp.	Calc.
3	325	309	M2, T(SiO$_4$)	318	R(SiO$_4$)	374	T(M2)	322	318	331
4	375	360	R(SiO$_4$)	376	R(SiO$_4$)	410	ν2	381	376	378
5	447	430	ν2	412	ν2	435	R(SiO$_4$)	421	411	455
6	615	594	ν4	595	ν4	592	ν4	609	595	603
7	897	876	ν3	922	ν3	920	ν3	927	922	886

Iishi1978: Iishi (1978); Chopelas1991: Chopelas (1991); Noel: (Noel et al. 2006); McKeown: McKeown et al. (2010); S2017: Stangarone et al. (2017)

reported data exhibit some inconsistencies, which could arise from polarization mixing or errors in both experimental and computational approaches.

For Raman spectra, there is a typical doublet consisting of two high-intensity modes in the Raman spectra between 800 and 880 cm^{-1}. The peak positions of this doublet, known to be a function of composition, have been widely used to determine olivine composition (Wang et al. 2004; Kuebler et al. 2006; Breitburg et al. 2018). For forsterite under static conditions (0 K, 0 GPa), the highest-intensity peak (DB1) is calculated to be 837.8 cm^{-1}, and the second peak (DB2) is 855.8 cm^{-1} (Fig. 5). A visualization of the DB1 is provided in Fig. 6. Both modes exhibit Ag symmetry, consistent with the literature.

For the mode assignment of vibrational spectra, energy considerations are crucial. The energy required to excite a phonon is the most for stretching, followed by bending, rotation, and translation. Bending movement changes the bond angle between two neighboring O atoms and a central cation while stretching changes the bond length. Typically, stretching modes require higher energy (i.e., higher wave number) than bending modes. The frequency of stretching vibrations is influenced by both atom mass and bond stiffness, with heavier atoms vibrating at lower frequencies. Stretching modes can be symmetric or asymmetric, with the latter usually having higher energy. Kuebler et al. (2006) have divided them into ranges of wave numbers < 400, 400–700, and 700–900 cm^{-1} for Raman. Others, like Breitburg et al. (2018), use 500 and 800 cm^{-1} as separating wavenumbers. In general, Raman-active phonons below 500 cm^{-1} are lattice modes, where SiO$_4$ tetrahedra act as rigid units and Mg2 translations mix with SiO$_4$ rotations and translations. Raman modes above 500 cm^{-1} primarily involve atomic displacements within the SiO$_4$ tetrahedra. Paques-Ledent and Tarte (1973) summarized that the infrared region of 800–1050 cm^{-1} corresponds to stretching vibrations of the SiO$_4$ tetrahedron, 650–475 cm^{-1} to the bending of SiO$_4$, and below 475 cm^{-1} are external modes mainly due to the vibrations of the MgO$_6$ octahedra.

For the static calculations in this work, mode assignments for infrared and Raman are summarized in Tables 5 and 6. Predicted vibration types from symmetry (Table 1) are used as a constraint, although the visualization of each mode shows extensive mode mixing, especially between translation and rotation. Lower modes are attributed to the translation of Mg cations and the rotation of SiO$_4$, with a boundary between 400 and 500 cm^{-1}. Many modes involve a combination of movements, making clear distinctions challenging. This is understandable due to the shared O atoms between Mg–O bonds and SiO$_4$ tetrahedra, leading to the perturbation of SiO$_4$ tetrahedra movements caused by Mg atoms.
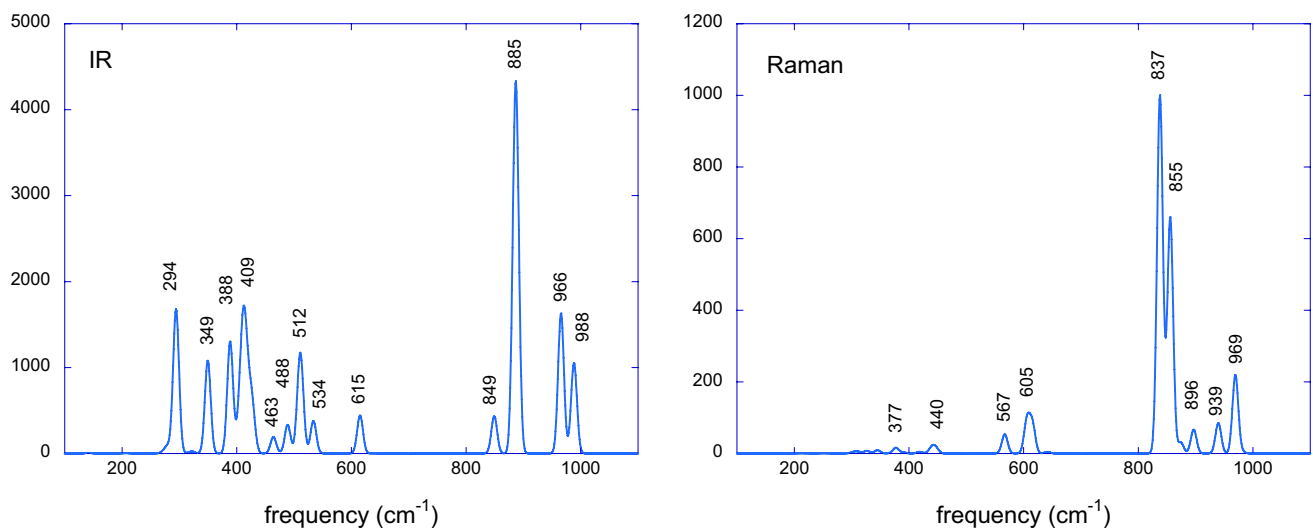
Fig. 5 Infrared (IR) and Raman spectra (relative intensity versus wavenumber) under static conditions
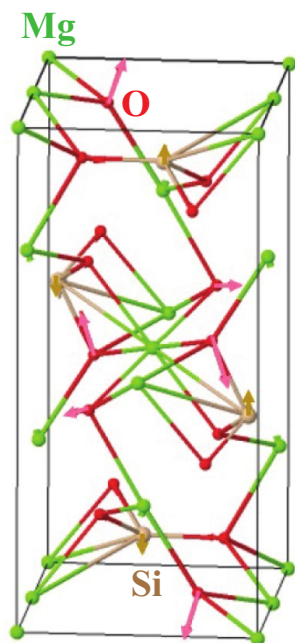

Fig. 6 The first peak of the Raman doublet at a frequency of 837.8 cm^{-1}. Symmetry Ag. Mg atoms are represented by green balls, O by red, and Si by apricot. Arrows depict the movement of each atom, if any. This mode is associated with the symmetric stretching of SiO$_4$, with the Si atom being approximately stationary (ν_1)

Pressure dependence of the vibrational frequencies for forsterite

The pressure dependence of vibrational frequencies is computed up to 15 GPa at 0 K, and the peak positions for infrared and Raman active modes are summarized in Tables 5 and 6. The infrared spectra exhibit a consistent pattern across different pressures, shifting to higher frequencies with increasing pressure (Figs. 7 and 8). Notably, they follow a generally linear trend, except for one B$_{1u}$ mode at 209.7 cm^{-1} for 0 GPa (Fig. 8). This mode barely changes its peak position with pressure. The linear fitting gives a slightly negative slope (-0.18 ± 0.29). For Raman, a similar trend is observed, albeit with some deviations. For instance, frequencies at 5 GPa are higher than those at 10 GPa, and four modes do not show a good linear trend (Fig. 8). All the four Raman modes deviating from linear trends share the symmetry of A$_g$. This rough linear trend agrees well with findings from literature studies. Chopelas (1990) and Wang et al. (1993) demonstrated that all Raman bands move to higher frequencies with increasing pressure, displaying a linear relationship for pressures up to ~7–9 GPa. Then, there is a decrease in the pressure derivative of some Raman modes. They attributed this change in slope to the compression mechanism change in forsterite under pressure, which may offer insights into the deviations observed in our study.

Except for one B$_{1u}$ mode being invariant with pressure, the pressure dependence dν_i/dP for infrared varies from 1.5 to 4.7 with an average of 3.0 ± 1.0 (σ) cm^{-1}/GPa. In the case of Raman, excluding the mode with a frequency of 211 cm^{-1} at 0 GPa, the dν_i/dP ranges from 0.6 to 4.8 with an average of 2.6 cm^{-1}/GPa. While there is no significant difference observed in dν_i/dP for low-frequency and high-frequency modes (Fig. 9), the relative frequency change (dν_i/ν_i/dP) shows a notably higher value for low-frequency modes compared to high-frequency modes. The isothermal mode Grüneisen parameter can be used to quantify the relative frequency change with pressure.
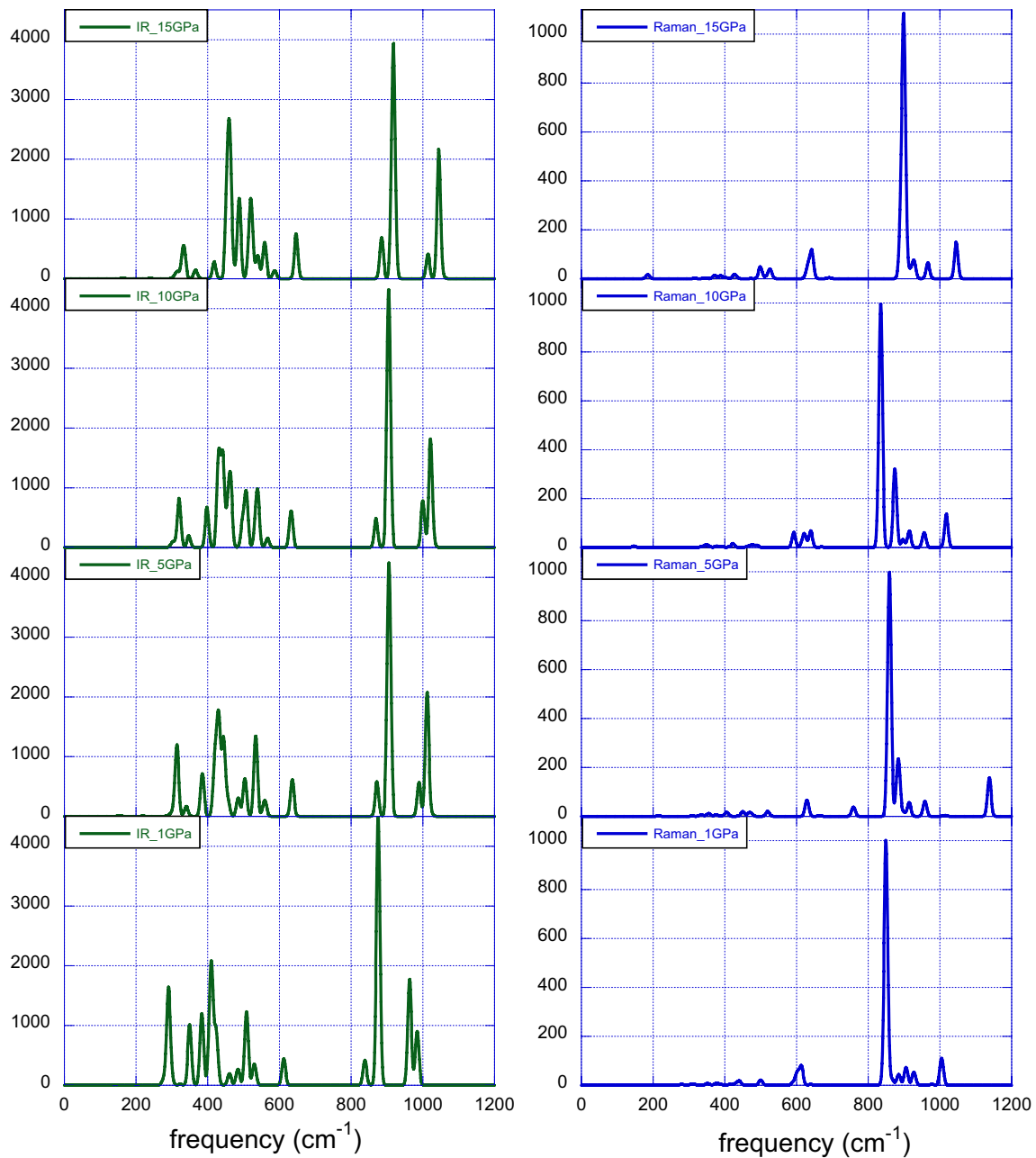
Fig. 7 Infrared (left) and Raman (right) spectra under various pressures up to 15 GPa, all at 0 K

The Grüneisen parameter connects the volume and vibrational frequencies directly. The ith vibrational mode of a crystal has a mode Grüneisen parameter γ_i, defined as

$$\gamma_i = -\frac{d\, \ln\nu_i}{d\, \ln V} \tag{10}$$

If we combine the definition of the bulk modulus and Eq. 9, the Grüneisen parameter of ith mode at a specific temperature (isothermal mode Grüneisen parameter) γ_{iT} can be written as

$$\gamma_{iT} = K_T \left(\frac{\partial \ln\nu_i}{\partial P} \right)_T \tag{11}$$

Similarly, if we combine the definition of thermal expansion coefficient with Eq. 9, the Grüneisen parameter of the ith mode at a given pressure P (isobaric mode Grüneisen parameter) can be written as

$$\gamma_{iP} = \frac{1}{\alpha} \left(\frac{\partial \ln\nu_i}{\partial T} \right)_P \tag{12}$$

Fig. 8 Linear frequency fitting with pressure. Four Raman modes (#4, 23, 24, and 35) are removed from the figure due to high scattering with pressure. All the four modes share the symmetry of Ag
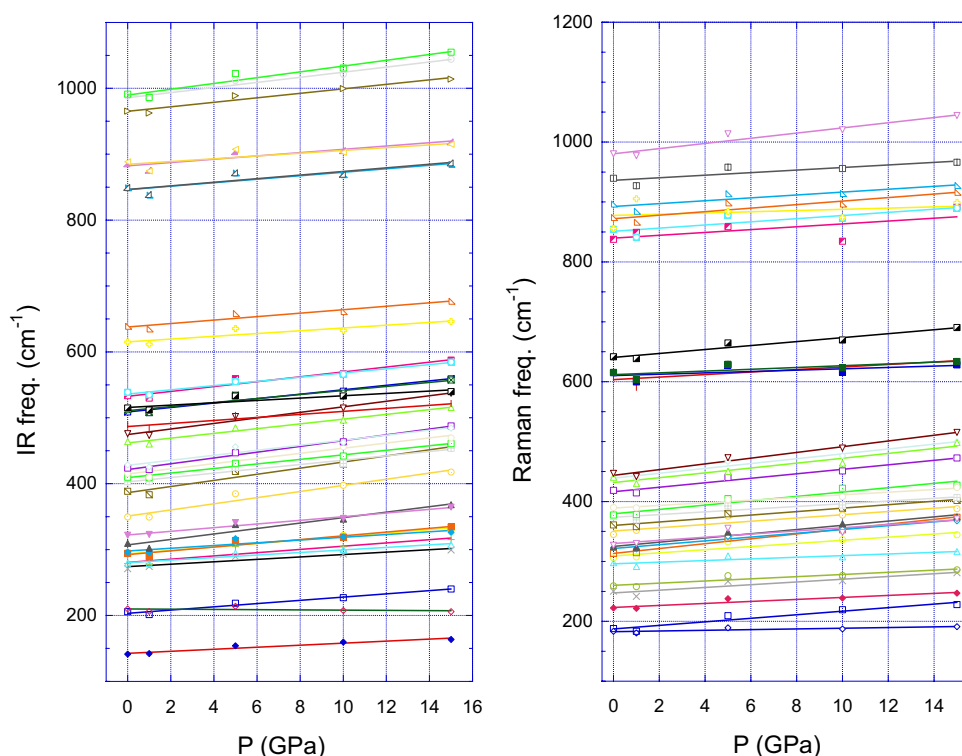
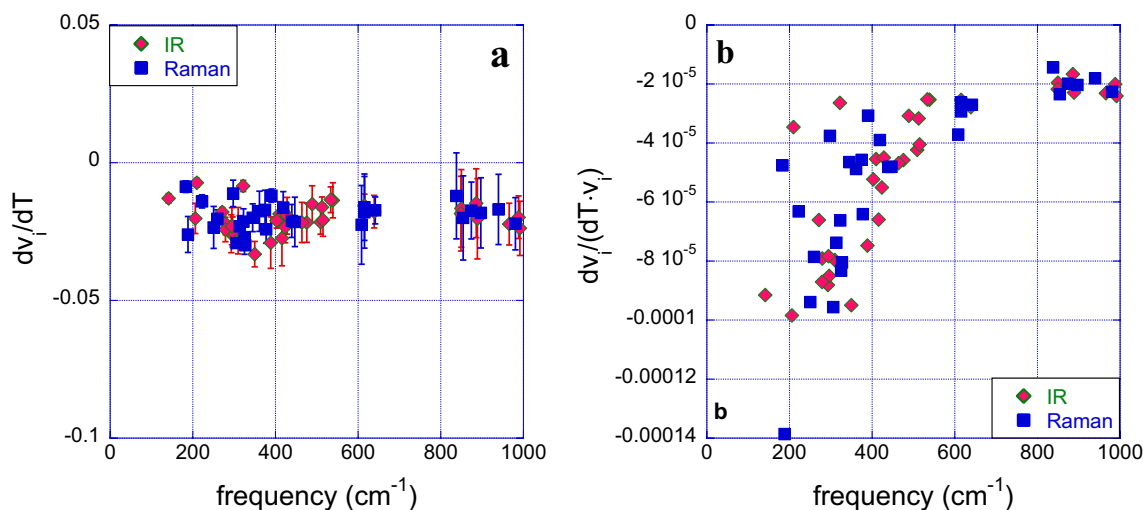**Fig. 9** **a** Infrared and Raman frequencies shift ($d\nu_i/dP$) with pressures, all at 0 K. The lowest frequency data for Raman is excluded. The frequency data in the plot is from 0 GPa. **b** The isothermal mode Grüneisen parameter (γ_{iT}) at 0 K. The bulk modulus of 123.3 GPa is used in this study. The frequency data in the figure is from 0 GPa. The two negative modes (one infrared, one Raman) are not shown
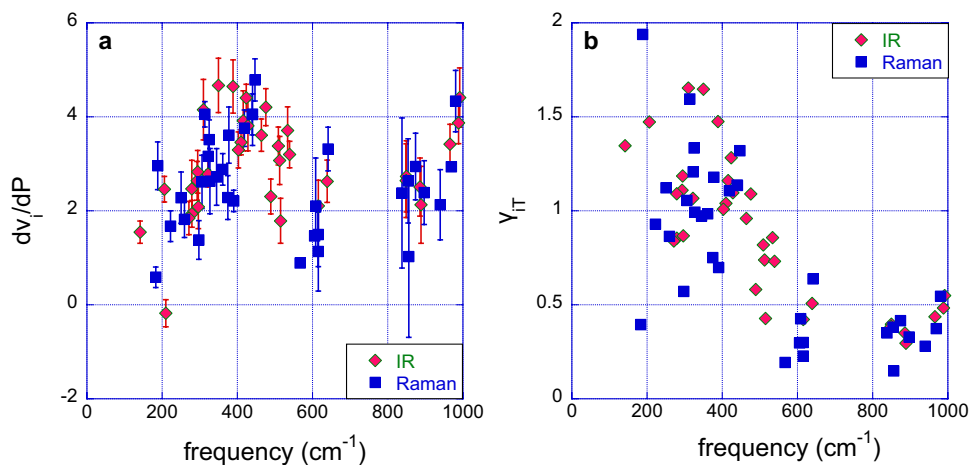
In the context of the QHA, vibrational frequencies are influenced by pressure and temperature solely through volume changes, therefore $\gamma_{iT} = \gamma_{iP}$ (Gillet 1996).

The isothermal mode Grüneisen parameter, γ_{iT}, is significantly smaller for modes above 600 cm^{-1}, corresponding to internal stretching and bending within the SiO$_4$ tetrahedra. Therefore, we can conclude that the internal movement of SiO$_4$ is less affected than the external lattice modes. This observation aligns with findings by Chopelas (1990), who attributed it to a more substantial volume change in the MgO$_6$ octahedra than the SiO$_4$ tetrahedra (Hazen 1976).

Temperature dependence of the vibrational frequencies for forsterite

The infrared and Raman vibrational modes for different temperatures are grouped based on their irreducible representation (symmetry). As the temperature increases, the frequency of each mode shifts to a lower wavenumber, displaying a generally linear relationship (Fig. 10). This trend aligns with findings in Raman studies from the literature (Gillet et al. 1991; Stangarone et al. 2017; Liu et al. 2021). No infrared spectra with increasing temperature have been reported, to our knowledge. For each mode, linear fitting was

Fig. 10 Linear frequency fitting with temperature. Four Raman modes (#21, 23, 24, and 31) are removed from the figure due to their non-linear trend with temperature. All four modes share the symmetry of A_g
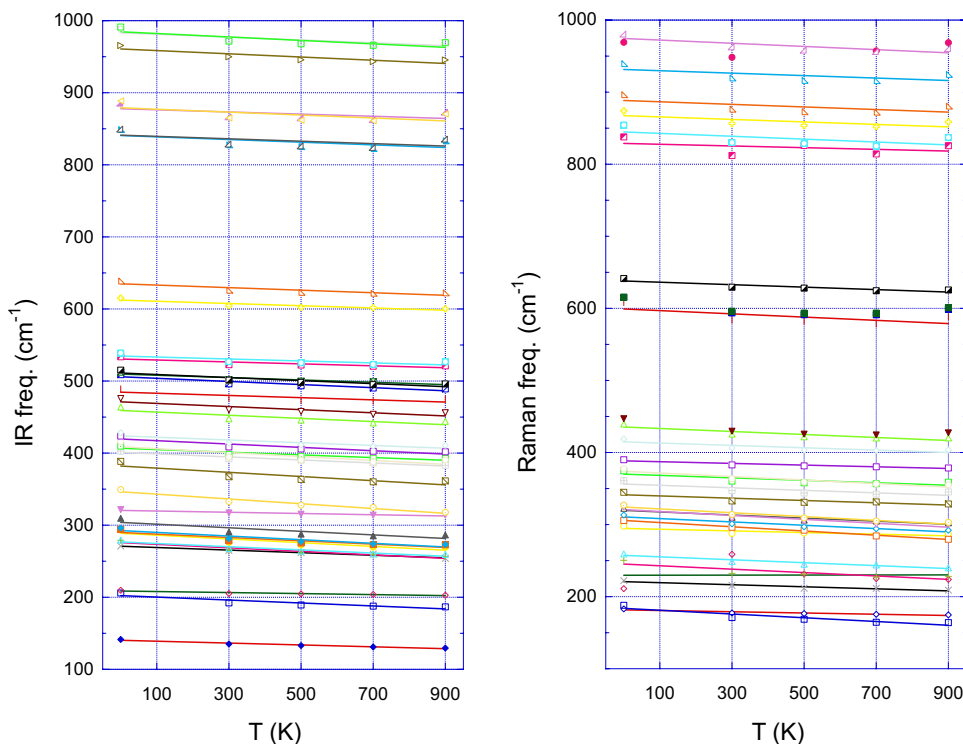
applied to assess the frequency shift with temperature $\Delta\nu_i/\Delta T$. The $\Delta\nu_i/\Delta T$ values for infrared range from -0.033 to -0.007 cm^{-1}/K, with an average of -0.020 ± 0.005 cm^{-1}/K (Fig. 11a). A few Raman modes deviate from a good linear trend. These outlier modes, characterized by A_g symmetry, are associated with the internal movement of SiO_4. The remaining Raman modes have $\Delta\nu_i/\Delta T$ values ranging from -0.029 to -0.009 cm^{-1}/K, averaging -0.019 ± 0.005 cm^{-1}/K (Fig. 11). These findings are consistent with reported

ranges of -0.029 to -0.008 cm^{-1}/K (average -0.017 cm^{-1}/K) in experimental studies by Gillet et al. (1991) and -0.024 to -0.005 cm^{-1}/K (average -0.016 cm^{-1}/K) in computational studies by Stangarone et al. (2017).

Similar to the pressure effect, the absolute frequency shift with temperature ($\Delta\nu_i/\Delta T$) does not show a dependence on frequencies (Fig. 11). However, the relative change, $\Delta\nu_i/\Delta T/\nu_i$, reveals that temperature has a more pronounced effect on lower frequencies associated with transition and

Fig. 11 **a** Infrared and Raman frequency shifts ($d\nu_i/dT$) with temperature. All pressures are 0 GPa. The lowest frequency data for Raman is excluded. **b** Relative frequency shifts with temperature ($d\ln\nu_i/dT$)

rotation than on the higher-frequency modes linked to the internal stretching and bending of SiO_4 (Fig. 11).

Vibrational frequencies of forsterite under simultaneous high *T* and *P* conditions

Simultaneous effects of temperature and pressure were simulated on vibrational modes for five pairs of *T* and *P*: (1000 K, 5 GPa), (1500 K, 10 GPa), (1500 K, 5 GPa), (2000 K, 10 GPa), and (2000 K, 20 GPa). The infrared and Raman spectra are displayed in Fig. 12. Infrared spectra are similar for various temperature and pressure pairs in terms of peaks and relative intensities, with only the peak frequencies change with *T* and *P*. However, Raman spectra show more variability.

Compositional and isotope effect on vibrational frequencies

In order to examine the compositional effect, we computed IR and Raman vibrational frequencies for the forsterite-fayalite solid solution. To maintain the symmetry of olivine, we specifically simulated the spectra for $MgFeSiO_4$, where all four Fe ions are placed either in M1 or M2 sites within a unit cell. An important consideration is the spin states for Fe. We examined both low-spin and high-spin states for Fe in fayalite, and for the high-spin state, we considered both ferro- and antiferromagnetic configurations. Our energy computations reveal that fayalite with high-spin Fe is more than 180 kJ more favorable than low-spin fayalite per mol formula unit, and the antiferromagnetic spin configuration is 2.5 kJ more favorable than its ferromagnetic counterpart (Table 7). Furthermore, fayalite has been reported to be a noncollinear antiferromagnetic compound below a Neel temperature of approximately 65 K with Mossbauer spectroscopy and neutron diffraction studies (Santoro et al. 1966; Hayashi et al. 1987). Above the Neel temperature, it is paramagnetic. Therefore, high-spin Fe should be used in olivine calculations. Due to the close energy of antiferromagnetic and ferromagnetic structures and the simplicity of the ferromagnetic setting, we employed ferromagnetic configurations in our
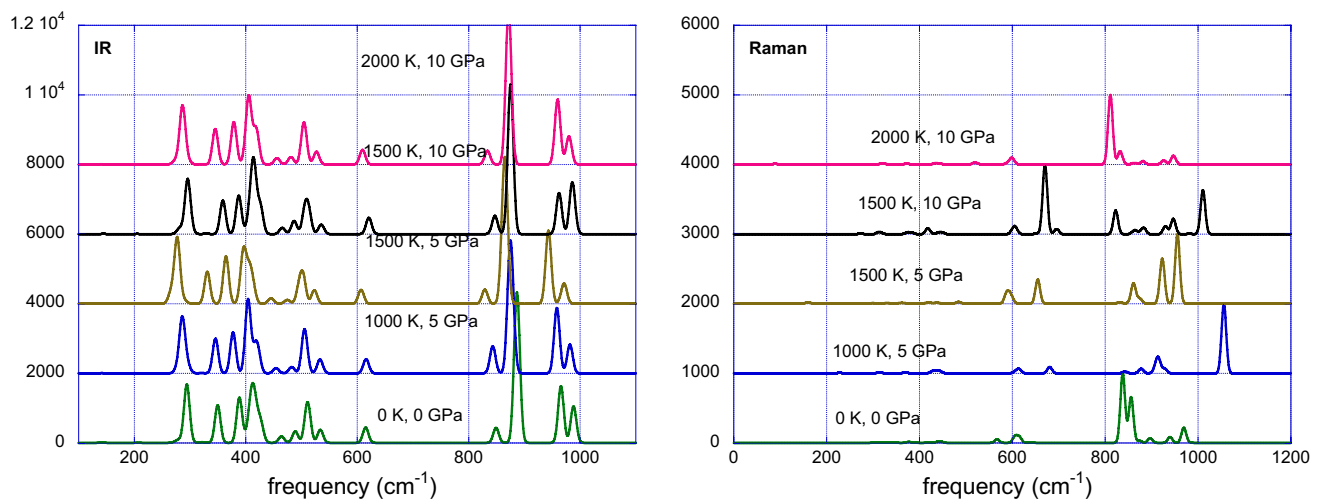

Fig. 12 Infrared and Raman spectra under simultaneous high temperatures and pressures

Table 7 Cell parameters and energetics calculation of olivine. All calculations started from the same structure

Composition	Spin of Fe	a (Å)	b (Å)	c (Å)	ΔME (kJ/(mol/f.u.))
Fe_2SiO_4	FM	4.9330	10.4716	6.0469	0
Fe_2SiO_4	AFM	4.9219	10.5160	6.0305	$\Delta ME_{AFM-FM} = -2.5$
Fe_2SiO_4	LS, unrestricted	4.7159	10.0151	5.8545	$\Delta ME_{LS-HS} = 184$
Fe_2SiO_4	LS, restricted	4.6477	9.9543	5.8222	$\Delta ME_{LS-HS} = 182$
$MgFeSiO_4$ (Fe in M1)	FM	4.9288	10.4764	5.9402	
$MgFeSiO_4$ (Fe in M2)	FM	4.8487	10.4119	6.1459	
Mg_2SiO_4	N/A	4.8504	10.3381	6.0581	

FM Ferromagnetic, *AFM* antiferromagnetic, *LS* low spin, *f.u* formula unit mole. ΔME represents the mechanical energy difference

computations for fayalite and MgFeSiO$_4$ for the IR and Raman spectra.

All vibrational modes in fayalite exhibit lower frequencies than their respective counterparts in forsterite (see Fig. 13 for infrared spectra), potentially caused by the different masses of Fe and Mg, changes in the cell parameters of fayalite and forsterite, or chemical/electronic differences of the two cations or their respective bonds to O atoms. The differences range from -8 to -126 cm^{-1}, with a slightly more pronounced distinction for higher frequency modes. In the calculations for the MgFeSiO$_4$ solid solutions, intermediate frequencies are observed compared to the two end members. However, for the same composition, the two configurations (Fe in M1 or M2 sites) exhibit different frequency modes, with $\Delta\nu_i$ from 28 to -41.5 cm^{-1}.

To isolate the mass effect on vibrational frequencies, we assigned different isotopes for metal cations. The default isotope for Mg used in the frequency calculations of Crystal17 is ^{24}Mg. We replaced all eight cations in the unit cell with a mass of 24 with isotopes 26 or 56. It's important to note that there is no mass of 56 for Mg. The calculations used here allow us to separate out the mass effect by artificially increasing the mass of Mg to 56 while maintaining Mg chemistry. Both calculations maintained the same crystal structure as forsterite with the default ^{24}Mg, differing only in isotope composition. The results indicate that ^{26}Mg shifted wavenumbers up to 12 cm^{-1} lower (Fig. 14). High vibrational frequencies (> 800 cm^{-1}), attributed to Si–O vibrations, seem to be less impacted (within -1 cm^{-1}). The "^{56}Mg" substitution causes a more significant shift (up to 80 cm^{-1}) than ^{26}Mg due to a more considerable mass difference. For low-frequency modes, the $\Delta\nu_i$ could be as much as approximately -62.5 cm^{-1} due to the heavy mass.

The mass effect on vibrational frequencies is not a constant value across different modes, and the shift is not directly proportional to the mass difference. To quantify the isotope effect, we consider a simple diatomic molecule harmonic oscillator. The frequency (ν) can be calculated as $\nu = \frac{1}{2\pi}\sqrt{k/\mu}$ with $\mu = \frac{m_1 m_2}{m_1 + m_2}$ representing the reduced mass and k as the force constant. In the case of metal cations bonded to O atoms (with a default mass of 16) to form octahedral sites, assuming the force constant remains constant, ν is approximated as $\sqrt{1/\mu} = \sqrt{\frac{m_1 + m_2}{m_1 m_2}} = \sqrt{\frac{m_1 + 16}{16 m_1}}$. For each mode, the frequency with ^{24}Mg is 1.016 times that of ^{26}Mg and 1.139 times that of ^{56}Fe (Fig. 15).
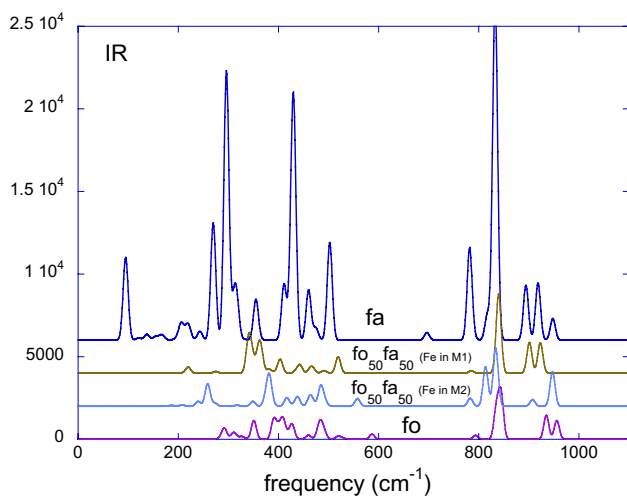

Fig. 13 IR vibrational frequencies for forsterite (fo)-fayalite (fa) solid solutions
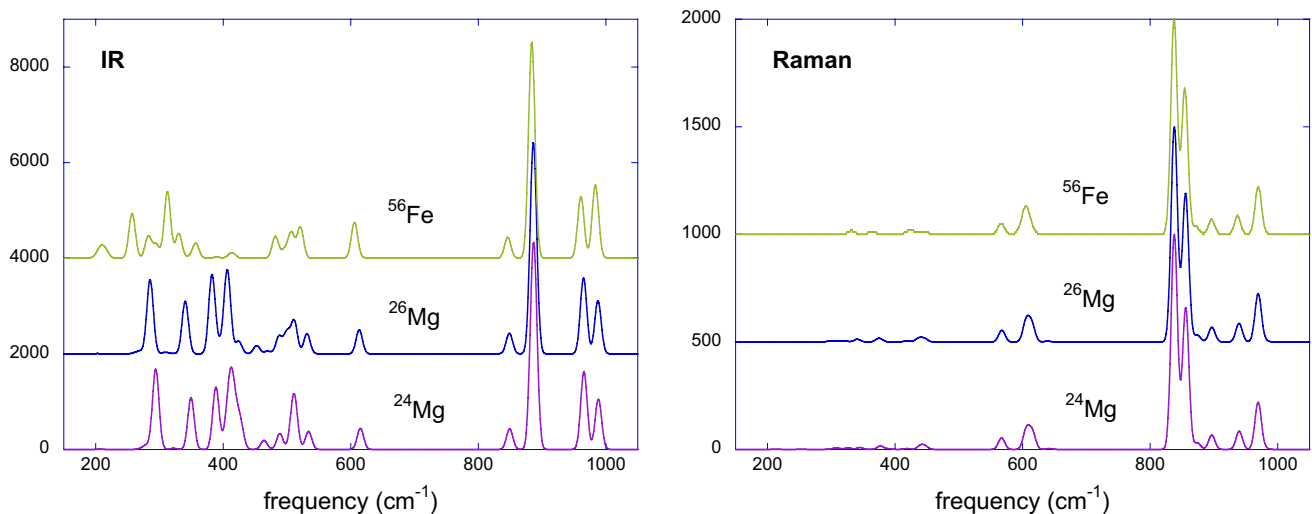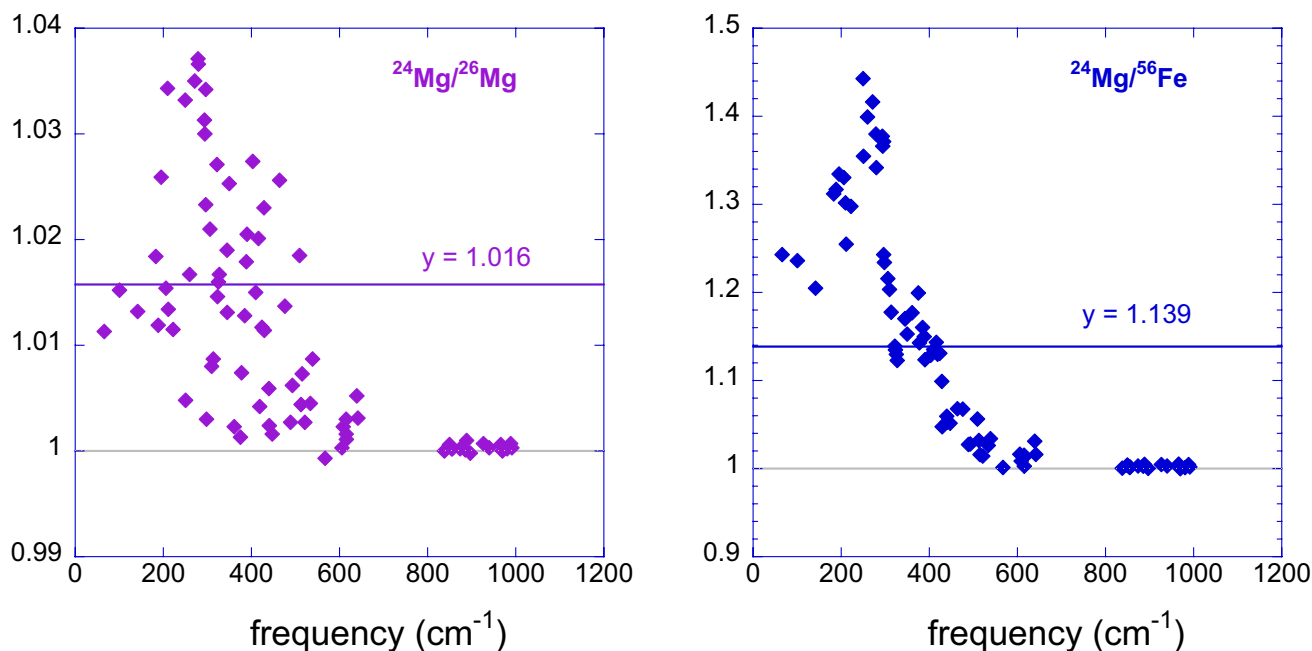

Fig. 14 Vibrational frequencies change due to the isotope effect. All three calculations have the same cell parameters and coordinates but different masses in all eight cations in the unit cell. The intensities of ^{56}Fe and ^{26}Mg shift up for better visualization

Fig. 15 Vibration frequencies change due to the isotope effect. All three calculations have the same cell parameters and coordinates but different masses. The isotope substitution applies to all eight cations in the unit cell

The lighter frequencies in fayalite compared to forsterite result from a combined effect of mass and cell parameter differences. By isolating the mass effect, it becomes possible to assess the percentage contribution of each factor. Specifically, the mass effect accounts for approximately 50% for the low-frequency modes and significantly lower percentages for high-frequency modes (Fig. 16). The cation substitution in octahedral sites primarily impacts the vibration of MO_6 and has a lesser effect on SiO_4. Although metal ions affect SiO_4 vibrations due to shared oxygen atoms, the influence is comparatively minor.

Discussions and implications

The vibrational properties of infrared and Raman are influenced by factors such as composition, temperature, pressure, isotope, spin, etc. In this study, we evaluate the effects of temperature and pressure in detail and briefly examine the compositional and cation distribution effects. The findings reveal significant impacts on normal modes, particularly the peak positions of certain vibrational modes like the doublet Raman modes. These modes have been used to predict olivine compositions. For instance, forsteritic (high molar $Mg/(Mg + Fe)$) olivine is indicative of a primitive magma source, while more fayalitic olivine suggests a more evolved source. However, caution should be taken in cases of substantial temperature and pressure variations. The two end-members of $(Fe, Mg)_2SiO_4$ show an approximate difference
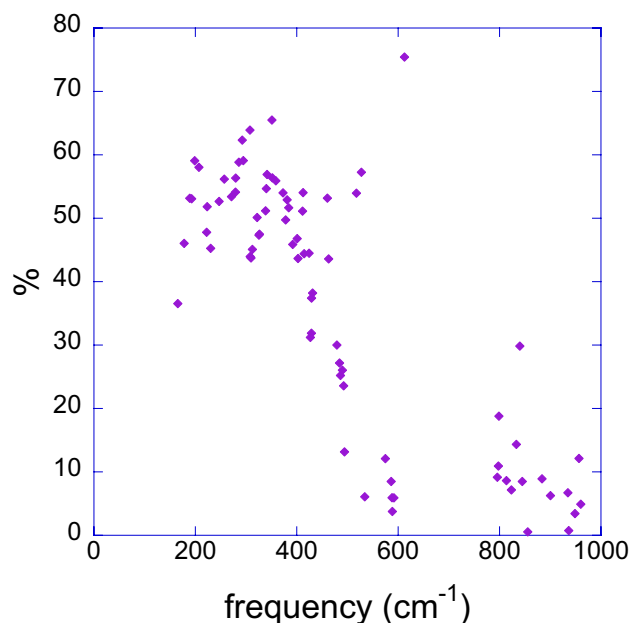

Fig. 16 The contribution of mass difference to the mode shift between forsterite and fayalite. The observed difference in vibrational modes between the two is influenced by a combined effect of mass difference and cell parameters

of 10 cm^{-1} for the doublet modes. Assuming an average of $\Delta\nu_i/\Delta T$ of -0.02 cm^{-1} K^{-1} and $\Delta\nu_i/\Delta P$ of 3 cm^{-1} GPa^{-1}, a 500 K temperature difference or 3 GPa pressure difference can completely override the composition indication if

failing to consider the temperature and pressure effects. The surface temperature of Mars may vary by 200 K, leading to a potential 40% error in composition identification when using Raman to analyze mineral compositions or structures on the Martian surface. An alternative approach, yet to be tested widely, could involve using lower frequencies controlled by substitution. However, these are challenging to measure due to the relatively low intensities of these modes. Advances in experimental techniques may open avenues for broader applications in the future.

This study helps develop a more comprehensive data set of infrared and Raman spectra in temperature, pressure, and compositional space. The findings underscore the significant influence of factors such as temperature, pressure, composition, and cation ordering on peak positions. Frequency changes for each mode can be effectively parameterized using a simplified equation, enhancing our understanding of vibrational behavior in diverse temperature, pressure, and composition ranges as

$$dv_i = a_i dT + b_i dP + c_i X \qquad (13)$$

where X is the fractional contribution of fayalite in the olivine. This is a combined effect of temperature–pressure-composition ($P{-}T{-}X$). Or, if the specific occupation of iron on the two different cation sites is taken into account, this equation could be expanded to

$$dv_i = a_i dT + b_i dP + c_i X_{Fe}^{M1} + d_i X_{Fe}^{M2} \qquad (14)$$

The methodology employed in this study provides insights into the conditions under which specific phonons or vibrational modes are responsible for pronounced changes in thermal expansion and compression under pressure. This enhances our understanding of the intricate dynamics governing these phenomena.

Wide applications can also be found in the reported bulk modulus and thermal expansion data. One important application is in seismic data interpretation. Seismic wave velocities are influenced by the density and elastic properties of materials. The compressional-wave velocity $\left(V_p = \sqrt{\frac{K + \frac{4\mu}{3}}{\rho}} \right)$ and shear-wave velocity $\left(V_s = \sqrt{\frac{\mu}{\rho}} \right)$ are functions of bulk modulus K, shear modulus μ, and density ρ. While bulk modulus data has been reported in the literature, it is primarily at ambient conditions. However, olivine's bulk modulus varies significantly with pressure and temperature. Our study not only provides data under different temperature and pressure conditions but also offers linear/second-order polynomial fitting. This analytical form of the equation of state is valuable compared to discrete data points. Additionally, the bulk modulus data at high temperatures and pressures find applications in

equations of state, such as the third-order Birch-Murnaghan equation. The Birch–Murnaghan isothermal equation of state is usually used at room temperature. With the bulk modulus K and its derivative K' data at different temperatures, it can then be used for deep Earth conditions.

The methodology introduced in this study provides a systematic approach to compute infrared absorption and Raman spectra for minerals under simultaneous high temperature and high pressure, provided anharmonicity is not significant. Its applicability extends beyond olivine and can be effectively employed for studying other minerals as well.

Conclusions

We employed DFT in conjunction with the QHA to simulate the crystal structure change and vibrational properties of forsterite under high temperature and pressure conditions. Assuming the temperature is within the quasi-harmonic validity range, vibrational frequencies become solely dependent on the crystal structure, including both cell parameters and fractional positions. For a given temperature–pressure pair, we used QHA to obtain cell parameters, optimized the crystal structure, and computed infrared and Raman vibrational frequencies. This marks the first report, to our knowledge, of vibrational frequencies under simultaneous high-temperature and high-pressure conditions. A detailed examination of vibrational frequencies under varying temperature and pressure conditions reveals significant shifts in peak positions. The temperature- and pressure-induced frequency shifts vary for each mode, with an average of 3 cm^{-1}/GPa and -0.017 cm^{-1}/K. Caution is advised when interpreting olivine compositions based on peak positions, especially in the presence of significant changes in environmental conditions (temperature, pressure). In addition to the temperature and pressure effect, we also evaluated the compositional effect and isotopic effect on vibrational frequencies. This study contributes to the development of a comprehensive dataset for infrared and Raman spectra in temperature, pressure, and compositional space, enhancing our ability to predict and interpret olivine data across diverse planetary conditions.

Data availability All available data are given in the text and supplementary material.

Declarations

Conflict of interest The authors declare no competing interests.

References

Abramson EH, Brown JM, Slutsky LJ, Zaug J (1997) The elastic constants of San Carlos olivine to 17 GPa. J Geophys Res: Solid Earth 102:12253–12263. https://doi.org/10.1029/97JB00682

Akaogi M, Ross NL, McMillan P, Navrotsky A (1984) The Mg_2SiO_4 polymorphs (olivine, modified spinel and spinel)–thermodynamic properties from oxide melt solution calorimetry, phase relations, and models of lattice vibrations. Am Miner 69:499–512

Akimoto S-I, Akaogi M, Kawada K, Nishizawa O (1976) Mineralogic distribution of iron in the upper half of the transition zone in the earth's mantle. In: The Geophysics of the Pacific Ocean Basin and Its Margin. American Geophysical Union (AGU), pp 399–405

Allen PB (2020) Theory of thermal expansion: Quasi-harmonic approximation and corrections from quasi-particle renormalization. Mod Phys Lett B 34:2050025. https://doi.org/10.1142/S0217984920500256

Andrault D, Bouhifd MA, Itié JP, Richet P (1995) Compression and amorphization of $(Mg, Fe)_2SiO_4$ olivines: an X-ray diffraction study up to 70 GPa. Phys Chem Miner 22:99–107. https://doi.org/10.1007/BF00202469

Baroni S, Giannozzi P, Isaev E (2010) Density-functional perturbation theory for quasi-harmonic calculations. Rev Miner Geochem 71:39–57. https://doi.org/10.2138/rmg.2010.71.3

Besson JM, Pinceaux JP, Anastopoulos C, Velde B (1982) Raman spectra of olivine up to 65 kilobars. J Geophys Res: Solid Earth 87:10773–10775. https://doi.org/10.1029/JB087iB13p10773

Bostroem D (1987) Single-crystal X-ray diffraction studies of synthetic Ni-Mg olivine solid solutions. Am Miner 72:965–972

Bouhifd MA, Andrault D, Fiquet G, Richet P (1996) Thermal expansion of forsterite up to the melting point. Geophys Res Lett 23:1143–1146. https://doi.org/10.1029/96GL01118

Breitburg D, Levin LA, Oschlies A et al (2018) Declining oxygen in the global ocean and coastal waters. Science 359:eaam7240. https://doi.org/10.1126/science.aam7240

Carrier P, Wentzcovitch R, Tsuchiya J (2007) First-principles prediction of crystal structures at high temperatures using the quasiharmonic approximation. Phys Rev B 76:064116. https://doi.org/10.1103/PhysRevB.76.064116

Chen S (2022) A journey from partition coefficients in melt inclusions of lunar samples to the prediction of vibrational modes under high P/T conditions and the thermodynamics of sulfide-mediated redox reactions in sediments. Thesis

Cho Y, Böttger U, Rull F et al (2021) In situ science on Phobos with the Raman spectrometer for MMX (RAX): preliminary design and feasibility of Raman measurements. Earth Planets Space 73:232. https://doi.org/10.1186/s40623-021-01496-z

Chopelas A (1990) Thermal properties of forsterite at mantle pressures derived from vibrational spectroscopy. Phys Chem Miner 17:149–156. https://doi.org/10.1007/BF00199666

Chopelas A (1991) Single crystal Raman spectra of forsterite, fayalite, and monticellite. Am Miner 76:1101–1109

Cooney TF, Scott ERD, Krot AN et al (1999) Vibrational spectroscopic study of minerals in the Martian meteorite ALH 84001. Am Miner 84:1569–1576. https://doi.org/10.2138/am-1999-1010

Couvy H, Chen J, Drozd V (2010) Compressibility of nanocrystalline forsterite. Phys Chem Miner 37:343–351. https://doi.org/10.1007/s00269-009-0337-8

Dai RC, Ding X, Wang ZP, Zhang ZM (2013) Pressure and temperature dependence of Raman scattering of $MnWO_4$. Chem Phys Lett 586:76–80. https://doi.org/10.1016/j.cplett.2013.09.035

Deringer VL, Stoffel RP, Dronskowski R (2014) Vibrational and thermodynamic properties of GeSe in the quasiharmonic approximation. Phys Rev B 89:094303. https://doi.org/10.1103/PhysRevB.89.094303

Deshpande MP, Bhatt SV, Sathe V et al (2014) Pressure and temperature dependence of Raman spectra and their anharmonic effects in Bi2Se3 single crystal. Physica B 433:72–78. https://doi.org/10.1016/j.physb.2013.10.008

Dovesi R, Erba A, Orlando R et al (2018) Quantum-mechanical condensed matter simulations with CRYSTAL. Wires Comput Mol Sci 8:e1360. https://doi.org/10.1002/wcms.1360

Downs RT, Zha C-S, Duffy TS, Finger LW (1996) The equation of state of forsterite to 17.2 GPa and effects of pressure media. Am Miner 81:51–55. https://doi.org/10.2138/am-1996-1-207

Durben DJ, McMillan PF, Wolf GH (1993) Raman study of the high-pressure behavior of forsterite (Mg_2SiO_4) crystal and glass. Am Miner 78:1143–1148

Dyar MD, Sklute EC, Menzies ON et al (2009) Spectroscopic characteristics of synthetic olivine: an integrated multi-wavelength and multi-technique approach. Am Miner 94:883–898. https://doi.org/10.2138/am.2009.3115

Erba A (2014) On combining temperature and pressure effects on structural properties of crystals with standard ab initio techniques. J Chem Phys 141:124115. https://doi.org/10.1063/1.4896228

Erba A, Maul J, De La Pierre M, Dovesi R (2015a) Structural and elastic anisotropy of crystals at high pressures and temperatures from quantum mechanical methods: the case of Mg_2SiO_4 forsterite. J Chem Phys 142:204502. https://doi.org/10.1063/1.4921781

Erba A, Maul J, Itou M et al (2015b) Anharmonic thermal oscillations of the electron momentum distribution in lithium fluoride. Phys Rev Lett 115:117402. https://doi.org/10.1103/PhysRevLett.115.117402

Erba A, Shahrokhi M, Moradian R, Dovesi R (2015c) On how differently the quasi-harmonic approximation works for two isostructural crystals: thermal properties of periclase and lime. J Chem Phys 142:044114. https://doi.org/10.1063/1.4906422

Finkelstein GJ, Dera PK, Jahn S et al (2014) Phase transitions and equation of state of forsterite to 90 GPa from single-crystal X-ray diffraction and molecular modeling. Am Miner 99:35–43. https://doi.org/10.2138/am.2014.4526

Ghose S, Choudhury N, Chaplot SL, Rao KR (1992) Phonon density of states and thermodynamic properties of minerals. In: Saxena SK (ed) Thermodynamic data: systematics and estimation. Springer, New York, NY, pp 283–314

Gillet P (1996) Raman spectroscopy at high pressure and high temperature. Phase transitions and thermodynamic properties of minerals. Phys Chem Miner 23:263–275. https://doi.org/10.1007/BF00207767

Gillet P, Guyot F, Malezieux J-M (1989) High-pressure, high-temperature Raman spectroscopy of Ca_2GeO_4 (olivine form): some insights on anharmonicity. Phys Earth Planet Inter 58:141–154. https://doi.org/10.1016/0031-9201(89)90050-2

Gillet P, Richet P, Guyot F, Fiquet G (1991) High-temperature thermodynamic properties of forsterite. J Geophys Res: Solid Earth 96:11805–11816. https://doi.org/10.1029/91JB00680

Hayashi M, Tamura I, Shimomura O et al (1987) Antiferromagnetic transition of fayalite under high pressure studied by Mössbauer spectroscopy. Phys Chem Miner 14:341–344. https://doi.org/10.1007/BF00309807

Hazen RM (1976) Effects of temperature and pressure on the crystal structure of forsterite. Am Miner 61:1280–1293

Hazen RM (1977) Effects of temperature and pressure on the crystal structure of ferromagnesian olivine. Am Miner 62:286–295

Hofmeister AM (1987) Single-crystal absorption and reflection infrared spectroscopy of forsterite and fayalite. Phys Chem Miner 14:499–513. https://doi.org/10.1007/BF00308285

Hofmeister AM (1997) Infrared reflectance spectra of fayalite, and absorption datafrom assorted olivines, including pressure and isotope effects. Phys Chem Min 24:535–546. https://doi.org/10.1007/s002690050069

Iishi K (1978) Lattice dynamics of forsterite. Am Miner 63:1198–1208

Ito E, Katsura T (1989) A temperature profile of the mantle transition zone. Geophys Res Lett 16:425–428. https://doi.org/10.1029/GL016i005p00425

Karr C (1975) Infrared and Raman Spectroscopy of lunar and terrestrial minerals. Academic Press, Cambridge, pp 359–375

Katsura T, Ito E (1989) The system Mg_2SiO_4-Fe_2SiO_4 at high pressures and temperatures: precise determination of stabilities of olivine, modified spinel, and spinel. J Geophy Res: Solid Earth 94:15663–15670. https://doi.org/10.1029/JB094iB11p15663

Kayama M, Tomioka N, Ohtani E et al (2018) Discovery of moganite in a lunar meteorite as a trace of H_2O ice in the Moon's regolith. Sci Adv 4:eaar4378. https://doi.org/10.1126/sciadv.aar4378

Kolesov BA, Geiger CA (2004) A Raman spectroscopic study of Fe–Mg olivines. Phys Chem Miner 31:142–154. https://doi.org/10.1007/s00269-003-0370-y

Korablev OI, Dobrolensky Y, Evdokimova N et al (2017) Infrared spectrometer for ExoMars: a mast-mounted instrument for the rover. Astrobiology 17:542–564. https://doi.org/10.1089/ast.2016.1543

Kudoh Y, Takéuchi Y (1985) The crystal structure of forsterite Mg_2SiO_4 under high pressure up to 149 kb. Zeitschrift Für Kristallographie - Cryst Mater 171:291–302. https://doi.org/10.1524/zkri.1985.171.14.291

Kuebler KE, Jolliff BL, Wang A, Haskin LA (2006) Extracting olivine (Fo–Fa) compositions from Raman spectral peak positions. Geochim Cosmochim Acta 70:6201–6222. https://doi.org/10.1016/j.gca.2006.07.035

Kumazawa M, Anderson OL (1969) Elastic moduli, pressure derivatives, and temperature derivatives of single-crystal olivine and single-crystal forsterite. J Geophys Res 1896–1977(74):5961–5972. https://doi.org/10.1029/JB074i025p05961

Lalla EA, Konstantinidis M, Veneranda M et al (2022) Raman characterization of the CanMars rover field campaign samples using the Raman laser spectrometer exomars simulator: implications for Mars and Planetary exploration. Astrobiology 22:416–438. https://doi.org/10.1089/ast.2021.0055

Lam PK, Yu R, Lee MW, Sharma SK (1990) Structural distortions and vibrational modes in Mg_2SiO_4. Am Miner 75:109–119

Li L, Wentzcovitch RM, Weidner DJ, Da Silva CRS (2007) Vibrational and thermodynamic properties of forsterite at mantle conditions. J Geophys Res: Solid Earth. https://doi.org/10.1029/2006JB004546

Ling ZC, Wang A, Jolliff BL (2011) Mineralogy and geochemistry of four lunar soils by laser-Raman study. Icarus 211:101–113. https://doi.org/10.1016/j.icarus.2010.08.020

Liu L (1993) Volume, pressure and temperature dependences of vibrational frequencies. Phys Lett A 176:448–453. https://doi.org/10.1016/0375-9601(93)90477-H

Liu D, Guo X, Smyth JR et al (2021) High-temperature and high-pressure Raman spectra of $Fo_{89}Fa_{11}$ and $Fo_{58}Fa_{42}$ olivines: iron effect on thermodynamic properties. Am Miner 106:1668–1678. https://doi.org/10.2138/am-2021-7686

McKeown DA, Bell MI, Caracas R (2010) Theoretical determination of the Raman spectra of single-crystal forsterite (Mg_2SiO_4). Am Miner 95:980–986. https://doi.org/10.2138/am.2010.3423

Nestola F, Pasqual D, Smyth JR et al (2011) New accurate elastic parameters for the forsterite-fayalite solid solution. Am Miner 96:1742–1747. https://doi.org/10.2138/am.2011.3829

Noel Y, Catti M, D'Arco Ph, Dovesi R (2006) The vibrational frequencies of forsterite Mg_2SiO_4: an all-electron ab initio study with the CRYSTAL code. Phys Chem Miner 33:383–393. https://doi.org/10.1007/s00269-006-0085-y

Paques-Ledent MTh, Tarte P (1973) Vibrational studies of olivine-type compounds—I. The i.r. and Raman spectra of the isotopic species of Mg_2SiO_4. Spectrochim Acta, Part A 29:1007–1016. https://doi.org/10.1016/0584-8539(73)80140-0

Pascale F, Zicovich-Wilson CM, Orlando R et al (2005) Vibration frequencies of $Mg_3Al_2Si_3O_{12}$ Pyrope. An ab Initio Study with the CRYSTAL Code. J Phys Chem B 109:6146–6152. https://doi.org/10.1021/jp050316z

Poe BT, Romano C, Nestola F, Smyth JR (2010) Electrical conductivity anisotropy of dry and hydrous olivine at 8GPa. Phys Earth Planet Inter 181:103–111. https://doi.org/10.1016/j.pepi.2010.05.003

Rao KR, Chaplot SL, Choudhury N et al (1988) Lattice dynamics and inelastic neutron scattering from forsterite, Mg_2SiO_4: phonon dispersion relation, density of states and specific heat. Phys Chem Miner 16:83–97. https://doi.org/10.1007/BF00201334

Reynard B, Price GD, Gillet P (1992) Thermodynamic and anharmonic properties of forsterite, α-Mg_2SiO_4: computer modelling versus high-pressure and high-temperature measurements. J Geophys Res: Solid Earth 97:19791–19801. https://doi.org/10.1029/92JB01554

Rull F, Maurice S, Hutchinson I et al (2017) The Raman laser spectrometer for the ExoMars rover mission to Mars. Astrobiology 17:627–654. https://doi.org/10.1089/ast.2016.1567

Santoro RP, Newnham RE, Nomura S (1966) Magnetic properties of Mn_2SiO_4 and Fe_2SiO_4. J Phys Chem Solids 27:655–666. https://doi.org/10.1016/0022-3697(66)90216-2

Stangarone C, Böttger U, Bersani D et al (2017) Ab initio simulations and experimental Raman spectra of Mg_2SiO_4 forsterite to simulate Mars surface environmental conditions. J Raman Spectrosc 48:1528–1535. https://doi.org/10.1002/jrs.5127

Suzuki I, Anderson OL, Sumino Y (1983) Elastic properties of a single-crystal forsterite Mg_2SiO_4, up to 1200 K. Phys Chem Miner 10:38–46. https://doi.org/10.1007/BF01204324

Trots DM, Kurnosov A, Ballaran TB, Frost DJ (2012) High-temperature structural behaviors of anhydrous wadsleyite and forsterite. Am Miner 97:1582–1590. https://doi.org/10.2138/am.2012.3992

Trubitsyn AP, Trubitsyn VP (2020) Temperature distribution in the Earth's mantle. Dokl Earth Sci 495:905–909. https://doi.org/10.1134/S1028334X20120120

Valenzano L, Torres FJ, Doll K, et al (2006) Ab initio study of the vibrational spectrum and related properties of crystalline compounds; the case of $CaCO_3$ calcite. Z Phys Chem 220:893–912. https://doi.org/10.1524/zpch.2006.220.7.893

Valenzano L, Noël Y, Orlando R et al (2007) Ab initio vibrational spectra and dielectric properties of carbonates: magnesite, calcite and dolomite. Theor Chem Acc 117:991–1000. https://doi.org/10.1007/s00214-006-0213-2

Wang SY, Sharma SK, Cooney TF (1993) Micro-Raman and infrared spectral study of forsterite under high pressure. Am Miner 78:469–476

Wang A, Jolliff BL, Haskin LA (1995) Raman spectroscopy as a method for mineral identification on lunar robotic exploration missions. J Geophs Res: Planets 100:21189–21199. https://doi.org/10.1029/95JE02133

Wang A, Kuebler K, Jolliff B, Haskin LA (2004) Mineralogy of a Martian meteorite as determined by Raman spectroscopy. J Raman Spectrosc 35:504–514. https://doi.org/10.1002/jrs.1175

Wen X, Liang Y, Bai P et al (2017) First-principles calculations of the structural, elastic and thermodynamic properties of mackinawite (FeS) and pyrite (FeS$_2$). Physica B 525:119–126. https://doi.org/10.1016/j.physb.2017.09.007

Wentzcovitch RM, Yu YG, Wu Z (2010) Thermodynamic properties and phase relations in mantle minerals investigated by first principles quasiharmonic theory. Rev Mineral Geochem 71:59–98. https://doi.org/10.2138/rmg.2010.71.4

Wu Z, Wentzcovitch RM (2007) Vibrational and thermodynamic properties of wadsleyite: a density functional study. J Geophys Res: Solid Earth. https://doi.org/10.1029/2007JB005036

Zha C-S, Duffy TS, Downs RT et al (1996) Sound velocity and elasticity of single-crystal forsterite to 16 GPa. J Geophys Res: Solid Earth 101:17535–17545. https://doi.org/10.1029/96JB01266